REPORT DOCUMENTATION PAGE

AFRL-SR-AR-TR-02-

0354

Public reporting burden for this collection of information is estimated to average 1 hour per response, including the time for reviewing instruction, data needed, and completing and reviewing this collection of information. Send comments regarding this burden estimate or any other aspect of this burden to Department of Defense, Washington Headquarters Services, Directorate for Information Operations and Reports (0704-0188), 121 4302. Respondents should be aware that notwithstanding any other provision of law, no person shall be subject to any penalty for failing to comp valid OMB control number. PLEASE DO NOT RETURN YOUR FORM TO THE ABOVE ADDRESS.

1. REPORT DATE (DD-MM-YYYY) 23-09-2002	2. REPORT TYPE Final Technical Report		3. DATES COVERED (From - To) 15 April 1999 - 28 February 2002
4. TITLE AND SUBTITLE On the Transport of Polarized Infrared Signals Through the Terrestrial Atmosphere			5a. CONTRACT NUMBER F49620-99-C-0019
			5b. GRANT NUMBER
			5c. PROGRAM ELEMENT NUMBER
6. AUTHOR(S) Mark Pesses, Steven Israel, Rodney Meyer, Michael J. Price			5d. PROJECT NUMBER
			5e. TASK NUMBER
			5f. WORK UNIT NUMBER
7. PERFORMING ORGANIZATION NAME(S) AND ADDRESS(ES) Science Applications International Corporation 4001 Fairfax Drive, Suite 450 Arlington, VA 22203			8. PERFORMING ORGANIZATION REPORT NUMBER
9. SPONSORING / MONITORING AGENCY NAME(S) AND ADDRESS(ES) Air Force Office of Scientific Research 4015 Wilson Blvd. Mail Stop #713 Arlington, VA 222-3-1954			10. SPONSOR/MONITOR'S ACRONYM(S) AFOSR/NM
			11. SPONSOR/MONITOR'S REPORT NUMBER(S)

12. DISTRIBUTION / AVAILABILITY STATEMENT
Unrestricted

Approved for public release, distribution unlimited

13. SUPPLEMENTARY NOTES

14. ABSTRACT
Both the Mie scattering and polarimetric transport models indicate that, in the LWIR, the atmospheric effect on the transport of right-hand circularly polarized signals and left-hand circularly polarized signals is identical. In the LWIR, the observed normalized circular polarization anisotropy, S3/S0, of a signal should not require any atmospheric corrections. Because natural LWIR light in not circularly polarized, only an active system will be able to exploit this finding. Both the Mie scattering and polarimetric transport models indicate that, in the LWIR, the atmospheric effect on the transport of the two orthogonal components of linearly polarized signals should be significantly different. In the LWIR both the observed degree of lineal polarization and the observed normalized linear polarization anisotropy S1/S0 of a signal should require atmospheric corrections.

20021126 094

15. SUBJECT TERMS
Remote Sensing, LWIR, Polarization, Atmospheric Transport

16. SECURITY CLASSIFICATION OF:			17. LIMITATION OF ABSTRACT	18. NUMBER OF PAGES	19a. NAME OF RESPONSIBLE PERSON Mark Pesses
a. REPORT UNCLASSIFIED	b. ABSTRACT UNCLASSIFIED	c. THIS PAGE UNCLASSIFIED	None	80	19b. TELEPHONE NUMBER (include area code) (703) 276-3119

Standard Form 298 (Rev. 8-98)
Prescribed by ANSI Std. Z39.18

On The Transport of Polarized Infrared Signals
Trough the Terrestrial Atmosphere ·

Mark Pesses
Steven Israel
Rodney Meyer
Michael J. Price

Science Applications International Corporation
4001 Fairfax Drive, Suite 450
Arlington, VA 22203

September 2002

Table of Contents

Appendices Table of Contents

EXECUTIVE SUMMARY

In military remote sensing the successful exploitation of CCD defeating countermeasures, like hyperspectral and spectropolarimetric imaging, requires the accurate removal from image cubes of atmospheric effects. Such corrections require accurate atmospheric profile data that can be difficult or impossible to obtain empirically over enemy locations of interest. The purpose of the study reported on here in is to search for polarimetric signal parameters that are not effected by atmospheric transport and hence do not require the acquisition of auxiliary atmospheric profile data. That search was carried out by using both Mie scattering theory and a newly developed model for the atmospheric transport of polarized IR signals.

Both the Mie scattering and polarimetric transport models indicate that, in the LWIR, the atmospheric effect on the transport of right-hand circularly polarized signals and left-hand circularly polarized signals is identical.

This means that in the LWIR, the observed normalized circular polarization anisotropy, S3/S0, of a signal should not require any atmospheric corrections. Because natural LWIR light in not circularly polarized, only an active system will be able to exploit this finding.

On the other hand, both the Mie scattering and polarimetric transport models indicate that, in the LWIR, the atmospheric effect on the transport of the two orthogonal components of linearly polarized signals should be significantly different.

This means that in the LWIR, the observed degree of lineal polarization, $\sqrt{S_1^2 + S_2^2}/S_0$, and the observed normalized linear polarization anisotropy, S1/S0, of a signal should both require atmospheric corrections.

1.0 Introduction

In military remote sensing the measure→ countermeasure → counter-countermeasure spiral is a major driver of imaging technology. For example, monochromatic imaging which reliably identifies out-in-the-open targets can be countered by camouflage, which in turn can be countered with hyperspectral imaging, which in turn can be countered by hiding under trees or in heavy clutter, which in turn appears to be countered with spectropolarimetric imaging techniques.

Successful exploitation of these CCD defeating counter-countermeasures requires the accurate removal from the images cubes of the effects of atmospheric absorption, emission, and scattering. And before these corrections can be accurate performed atmospheric signal path profiles are required for density, pressure, temperature, humidity, chemical composition, particulate composition, and particulate size distribution. However, many of the required atmospheric profiles are difficult to obtain empirically except for the case of field experiments.

For hyperspectral data, AFRL's MODTRAN code can be used to calculate atmospheric transport effects and provide model atmospheric profiles in the absence of empirical data. While in FY03 a new version of MODTRAN will provide polarimetric sky shine data. There is currently no available DOD or NASA validated spectropolarimetric atmospheric transport models. The transition from modeling the atmospheric transport of hyperspectral signals to spectropolarimetric signals are from trivial. What is modeled for hyperspectral signals is the transport through the atmosphere of the wavelength dependence of the intensity of the electric field which has the units of energy and is a scalar. While what is modeled for spectropolarimetric signals is the transport through the atmosphere of the wavelength dependence of both the magnitude and phase angel correlation of the orthogonal components of the electric field vector. The absence of a "conservation of polarization" law for electromagnetic fields further complicates the development of a vector atmospheric transport model.

The primary purpose of the research reported on below, is to do an "end run" around this problem by searching for scalar spectropolarimetric parameters that, at least to first-order, would not require atmospheric corrections. The existence of such "correctionless" parameters greatly facilitates the use of unmanned platforms to in real time detect anomalies and objects of interest. The search is carried out in the 8 to 14 μm LWIR region for two reasons. First, at these wavelengths the air molecules have insignificant scattering cross-sections. Second, a system operating at these wavelengths has day-night capabilities.

The Final Report on this work is organized as follows: Coordinate Systems and Polarimetry Nomenclature in Section 2; Problem Background in Section 3; Statement of the Problem in Section 4; IR Atmospheric Transport Modeling in Section 5; Infrared Sky Brightness in Section 6; Modeling the Infrared Radiation Scattering Properties of Cirrus Clouds in Section 7; and, in Section 8, Application of Mie Scattering Theory to the Transport of Polarized LWIR Signals.

2.0 Coordinate Systems and Polarimetry Nomenclature

2.1 Propagating Plane Wave

The electric field vector $\mathbf{E}$ of the most general homogeneous plane wave propagating in along the positive z-axis of a Cartesian coordinate system is

$$\mathbf{E}(\omega, z, t) = \left(E_1(\omega) e^{i\delta_1(\omega)} \varepsilon_1 + E_2(\omega) e^{i\delta_2(\omega)} \varepsilon_2 \right) e^{iz - i\omega t} \tag{2.1}$$

where t is time, ω is angular frequency, E is real amplitude, δ is phase angel and ε_1 and ε_2 are both perpendicular to $\mathbf{z}$ and orthogonal to each other. If both components of $\mathbf{E}$ have the same phase angle ($\delta_1 = \delta_2$), the wave is linearly polarized. If both components of $\mathbf{E}$ have different phase angle ($\delta_1 \neq \delta_2$), the wave is elliptically polarized. If both components of $\mathbf{E}$ have same magnitude ($E_1 = E_2$) and differ in differ in phase angle by $\pm 90°$, the wave is circularly polarized and (2.1) becomes

$$\mathbf{E}(\omega, z, t) = E_0(\omega)(\varepsilon_1 \pm i\varepsilon_2) e^{iz - i\omega t} \tag{2.2}$$

where E_0 is the common real amplitudes. For an observer facing the incoming wave (negative $\mathbf{z}$ direction) and $\mathbf{E}$ is rotating in the counterclockwise direction, the sign term is positive and the wave left circularly polarized. Conversely if $\mathbf{E}$ is rotating in the clockwise direction, the sign term is negative and the wave right circularly polarized.

2.2 Stokes Parameters

The four Stokes parameters for the wave described by (2.1) and dropping the ω notation are

$$\begin{aligned}
S_0 &= E_1^2 + E_2^2 \\
S_1 &= E_1^2 - E_2^2 \\
S_2 &= 2E_1 E_2 \cos(\delta_2 - \delta_1) \\
S_3 &= 2E_1 E_2 \sin(\delta_2 - \delta_1)
\end{aligned} \tag{2.3}$$

If the wave is not circularly polarized $S_3 = 0$. The wave's normalized linear polarization anisotropy (LPA) is S_1 / S_0 and the degree of linear polarization (DOLP) is

$$\text{DOLP} = \sqrt{S_1^2 + S_2^2} / S_0 \tag{2.4}$$

Jackson, [1962] with the aid of complex orthogonal unit vectors reformulates (2.1) into

$$\mathbf{E}(\omega, z, t) = \left[E_+(\omega) \varepsilon_+ \pm E_-(\omega) \varepsilon_- \right] e^{iz - i\omega t} \tag{2.5}$$

where E_+ and E_- are the complex amplitudes and

$$\varepsilon\pm = 1/\sqrt{2}\,(\varepsilon_1 \pm i\varepsilon_2) \tag{2.6}$$

Elliptically polarized light can be represented by a $\pi/2$ out-of-phase right-handed and left-handed light. The four Stokes parameters for the wave described by (2.5) are

$$
\begin{aligned}
S_0 &= E_+^2 + E_-^2 \\
S_1 &= 2E_+E_-\cos(\delta_- - \delta_+) \\
S_2 &= 2E_+E_-\sin(\delta_- - \delta_+) \\
S_3 &= E_+^2 - E_-^2
\end{aligned}
\tag{2.7}
$$

If the wave is circularly polarized $S_1 = S_2 = 0$. The wave's normalized circular polarization anisotropy (CPA) is S_3/S_0.

The observational definitions of the Stokes components are given in (2.8)

$$
\begin{aligned}
S_0 &= I(0°,0) + I(90°,0) \\
S_1 &= I(90°,0) - I(0°,0) \\
S_2 &= I(45°,0) - I(135°,0) \\
S_3 &= I(45°,\pi/2) - I(135°,\pi/2)
\end{aligned}
\tag{2.8}
$$

where I is the observed intensity as a function of the linear polarization filter angle (the left-hand value inside parentheses) and the quarter-wave plate phase retardance (the right-hand value). Here, the $0°$ linear polarizer setting is parallel to ε_1 and in the positive direction, and value of the angle increase in the counterclockwise sense. To fully determine the value of the first three Stokes parameters require a set of four measurements with linear polarizers. To fully determine the value of the fourth the Stokes parameter requires two additional sets of measurements with quarter wave plates.

2.3 Natural Light and Coherence
Natural sources of light consist of a linear superposition of individual light waves. The resultant wave, given by (2.9) is rarely full polarized, and instead is usually partially polarized or unpolarized.

$$\mathbf{E}(\omega,z,t) = \left(\mathbf{E}_a(\omega,t)e^{i\delta_a(\omega,t)}\varepsilon_a + \mathbf{E}_b(\omega,t)e^{i\delta_b(\omega,t)}\varepsilon_b\right)e^{iz - i\omega t} \tag{2.9}$$

The Born and Wolf [1959] coherence matrix provides a statistical description of both natural and man made light. The four components of the Born and Wolf coherence matrix $\breve{\mathbf{J}}$ which is defined in (2.10)

3

$$J_{ab}(\omega, z) = \frac{1}{T}\int_0^T E(\omega, z, t) \bullet \varepsilon_a \; E^*(\omega, z, t) \bullet \varepsilon_b \, dt \qquad (2.10)$$

where the superscript "*" denotes complex conjugant and the integration time $T \gg 2\pi/\omega$. Substituting (2.9) into (2.10) and with no loss of generality replacing ω with wavelength λ gives,

$$J_{ab}(\lambda) = \frac{1}{T}\int_0^T E_a(\lambda, t) E_b(\lambda, t) e^{i\left(\delta_a(\lambda, t) - \delta_b(\lambda, t)\right)} dt \qquad (2.11)$$

The relationships between the Stokes parameters, the Born Wolf parameters, and their associated observations will be derived for the sake of simplicity in the Fresnel coordinate frame of reference. This is the coordinate system in which Fresnel's equations for reflection and transmission are valid. And this is also the coordinate system that the boundary conditions for Maxwell's equations are evaluated and in. It is important to note that Fresnel coordinate system is not globally defined, but locally defined by two unit vectors **n** and **k**, where **n** is the surface normal of the reflecting – transmitting boundary, and **k** is the propagation direction the electromagnetic wave. In the Fresnel coordinate system, shown in Figure 2.1, one component of **E** is perpendicular to both **n** and **k** and given by **Es = k x n**, and the other component of **E** is perpendicular to both **Es** and **k** and given by **Ep = Es x k.**

In the Fresnel coordinate system the "a" and "b" in (2.9) and (2.10) become "s" and "p". And the relations between the Stokes and Born Wolf parameters are given by (2.12) and 2.13)

$$
\begin{aligned}
S_0 &= J_{PP} + J_{SS} \\
S_1 &= J_{PP} - J_{SS} \\
S_2 &= J_{PS} + J_{SP} \\
S_3 &= i\left(J_{PS} - J_{SP}\right)
\end{aligned}
\qquad (2.12)
$$

$$
\begin{aligned}
J_{PP} &= (S_0 + S_1)/2 \\
J_{SS} &= (S_0 - S_1)/2 \\
J_{SP} &= (S_2 + i S_3)/2 \\
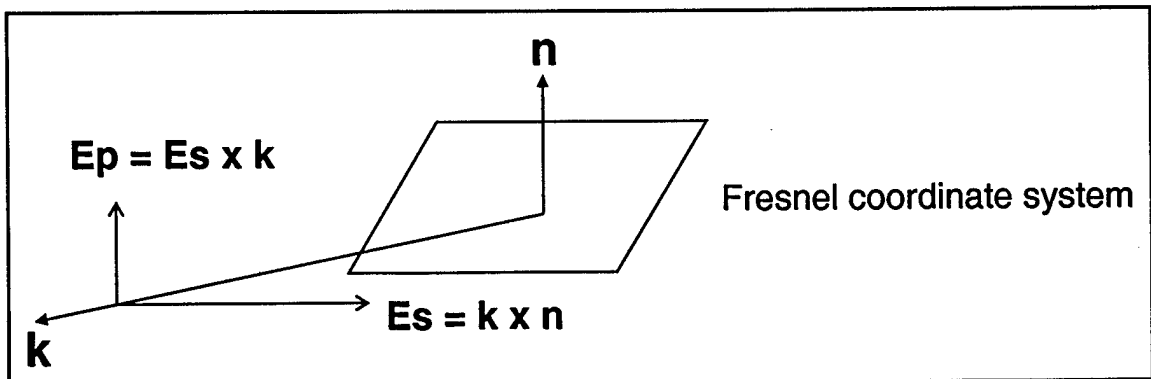J_{PS} &= (S_2 - i S_3)/2
\end{aligned}
\qquad (2.13)
$$

Figure 2.1 The coordinate system where the Fresnel equations are valid

4

The Born Wolf parameters can be expressed in terms of observations by substituting (2.8) into (2.13).

$$J_{SS} = I(0°,0)$$
$$J_{PP} = I(90°,0)$$
$$J_{SP} = \tfrac{1}{2}\left[I(45°,0) - I(135°,0)\right] + \tfrac{1}{2}i\left[I(45°,\pi/2) - I(135°,\pi/2)\right]$$
$$J_{PS} = \tfrac{1}{2}\left[I(45°,0) - I(135°,0)\right] - \tfrac{1}{2}i\left[I(45°,\pi/2) - I(135°,\pi/2)\right]$$

(2.14)

Comparing (2.14) to (2.8) shows that all the Stokes parameters are real, while two of the four Born Wolf parameters can be complex..

3.0 Background

3.1 Origins of IR Spectropolarimetry

The earliest know study of LWIR spectropolarimetry was in 1824, when Arago, [1824] reported that the glow emitted by hot incandescent metals is polarized. Sixty years later, Milliken, [1895] published papers on his research into the polarization of light emitted by incandescent solid and liquid surfaces. The study of optical polarization applied to remote sensing has it roots with Lyot, [1929] who built a non-imaging polarimeter with remarkable sensitivity. Infrared (IR) spectropolarimetry measurements were first made of astronomical objects in 1963 by Heiles and Drake, [1963]. By the 1960s, the characteristics of the polarization in the LWIR were already being modeled [Feofilov, 1961], and applied to natural targets [Hall Jr., 1964].

3.2 Hyperspectral Subpixel Demixing

Hyperspectral imaging currently provides a tool for detecting and determining the concentration of objects or chemical species embedded in complex backgrounds. Objects that are unresolved spatially can be detected on the subpixel level using the technique of linear demixing [Adams et. al., 1989; Gillespie, et. al., 1993; Boardman, 1993; Pesses and Stewart, 1997]. This technique assumes that the intensity spectrum of each individual pixel can be represented by a linear mixture of the intensity spectra of the objects or chemical species within the pixel provided that the number of spectral bands is greater than the number of objects or chemical species, i.e., number of subpixels. The subpixel demixing process finds the linear superposition of laboratory or ground truth reflectance spectra that most closely match the observed radiance spectra after atmospheric and geometric effects has been removed. The reliability and timeliness of hyperspectral target identification process depends in large part on the accuracy and speed at which the atmospheric corrections are made. This can be a liability because the accurate modeling requires knowledge of the distribution of atmospheric gasses and particles along both the Sun-target and the target-sensor. In addition, reflectance spectra can have light source – target – observer angle dependence due to polarization effects, for which corrections are also required.

The addition of polarization data provides in principle four independent methods for estimating the species concentration coefficients. Each of the four components of the Stokes' polarization vector can in principle be linear demixed. Subpixel demixing in the IR portion of the spectrum was first reported by Dozier, [1981] and more recently by Korb, et. al., [1996]; Pesses and Korb, [1997] and Pesses, et. al., [1998].

4.0 Statement of the Problem

As discussed in Section 1.0, before hyperspectral or spectropolarimetric remote sensing data can be reliably exploited it usually needs to be corrected for atmospheric propagation effects. We are currently not aware of any available atmospheric transport models for polarized IR signals. Current atmospheric transport models are for intensity only.

The primary purpose of the research reported here in is to search for scalar spectropolarimetric parameters that, at least to first-order, would not require atmospheric corrections. The existence of such "correctionless" parameters will greatly facilitate the use of unmanned platforms to in real time detect anomaly and objects of interest. The search is carried out in the 8 to 14 μm. LWIR region for two reasons. First, at these wavelengths the air molecules have insignificant scattering cross-sections. Second, a system operating at these wavelengths has day-night capabilities.

The basic hypothesis of this research is that in the LWIR neither the normalized linear polarization anisotropy nor the normalized circular polarization anisotropy are significant affected by atmospheric transport under most atmospheric conditions

$$LPA(\lambda) = \frac{S_1(\lambda)}{S_0(\lambda)} = \frac{I_P(\lambda) - I_S(\lambda)}{I_P(\lambda) + I_S(\lambda)} \tag{4.1}$$

$$CPA(\lambda) = \frac{S_3(\lambda)}{S_0(\lambda)} = \frac{I_R(\lambda) - I_L(\lambda)}{I_R(\lambda) + I_L(\lambda)} \tag{4.2}$$

Here, $I_P(\lambda)$ and $I_S(\lambda)$ are the intensity of S and P components of light at wavelength λ, and $I_R(\lambda)$ and $I_L(\lambda)$ are the intensity of right-handed and left-handed components of Slight at wavelength λ.

In general, scattering and absorption, processes in the atmosphere will attenuate the intensity of the s and p parts of the intensity by factors of x and y, respectively. Also, atmospheric emissions will contribute to the s and p parts of the intensity by amounts of α and β, respectively, so that the observed value of LPA is given by (ignoring the λ notation)

$$LPAO = \frac{yI_P - xI_S + \alpha - \beta}{yI_P + xI_S + \alpha + \beta} \tag{4.3}$$

And similarly, the scattering and absorption, processes in the atmosphere will attenuate the intensity of the r and h components by factors of v and w, respectively. And, atmospheric emissions will contribute to the r and h components by amounts of γ and ς, respectively, so that the observed value of CPA is given by (ignoring the λ notation)

6

$$CPAO = \frac{vI_R - wI_L + \gamma - \varsigma}{vI_R + wI_L + \gamma + \varsigma} \qquad (4.4)$$

The hypothesis to be tested is that the physics of scattering and absorption IR light in the terrestrial atmosphere under most conditions is nearly the same for s-type and p-type polarized light and, also nearly the same for right hand-type and left hand-type polarized light. If this hypothesis is true, then $y \approx x$ and $\gamma \cong \varsigma$. At LWIR wavelengths atmospheric emission is thermal and unpolarized so that $\alpha \cong \beta$ and $\gamma \approx \varsigma$. In this situation (4.3) and (4.4) reduced to

$$LPAO \approx \frac{I_P - I_S}{I_P + I_S + 2\alpha/x} \qquad (4.5)$$

$$CPAO \approx \frac{I_R - I_L}{I_R + I_L + 2\gamma/v} \qquad (4.6)$$

Expanding (4.5) and (4.6) in powers of $z = (2\alpha/x)/(I_P + I_S)$ and subtracting and $\rho = (2\gamma/v)/(I_R + I_L)$ respectively gives

$$LPAO \approx \frac{I_P - I_S}{I_P + I_S}\left(1 - \frac{2\alpha}{x(I_P + I_S)} + \frac{4\alpha^2}{x^2(I_P + I_S)^2}\cdots\right) \qquad (4.7)$$

$$CPAO \approx \frac{I_R - I_L}{I_R + I_L}\left(1 - \frac{2\gamma}{v(I_R + I_L)} + \frac{4\gamma^2}{v^2(I_R + I_L)^2}\cdots\right) \qquad (4.8)$$

The above hypothesis will be true provided that

$$1 \gg \frac{2\alpha}{x(I_P + I_S)} \qquad (4.9)$$

and
$$1 \gg \frac{2\gamma}{v(I_R + I_L)} \qquad (4.10)$$

At wavelengths equal to and shorter than IR radiation the terrestrial magnetic field is too weak to produce a measurable right to left polarization dependence is the absorption coefficient of atmospheric constituents [Jackson, 1962]. It addition, it seems reasonably likely that attenuation by scattering from randomly orientated atmospheric atoms, molecules and particulate should have little right to left or S to P polarization dependence. A similar case may be made for absorption of linearly polarized light by randomly orientated atoms, molecules and particulate. However, in clouds and precipitation fields ice crystals and water drops can have a preferred orientation. This could significantly affect the transport of polarized light.

5.0 LWIR Atmospheric Transport

5.1 Introduction

Our proposed research plan included two observational experiments to test the hypothesis that the physics of scattering and absorption IR light in the terrestrial atmosphere under most conditions is nearly the same for s-type and p-type polarized light and, also nearly the same for right hand-type and left hand-type polarized light. Both the surface propagation and airplane to ground propagation experiments included the use a 10.2 μm CO_2 laser at Kirtland AFB. Because of range safety issues neither of these experiments took place. We planed to replace the canceled active experiments with a passive experiment in Fall 2001 that used the sunlit surface of the Moon as the source of LWIR radiation. However, we ran into a terminal signal to noise problem because the field of view of our LWIR spectropolarimeter was five times larger then the angular diameter of the Moon. Therefore, we concentrated our remaining efforts on modeling the atmospheric transport of polarized LWIR signals. In March 2002, we found a rentable commercial instrument that should have work, but by then it was too late. Our observing procedures and data analysis techniques are discussed in Appendix B.

The primary objective of this section is to study theoretically if there are any significant differences in how the P and S components of right-hand and left-hand components of IR light are scattered and absorbed by the terrestrial atmosphere. Overhead remote sensing techniques for target analysis based on the measurement of polarization effects will necessarily involve understanding the atmospheric contribution. For an ordinary day, the atmosphere's natural radiation will be scattered from both air molecules and residual aerosol particles, with their relative importance being dependent upon the wavelength of interest. For ultraviolet and visible radiation, molecular scattering dominates over aerosol scattering while the converse is true for all infrared radiation. For particle sizes significantly smaller than the wavelength of the incident radiation - the situation of prime interest - scattering will be according to Raleigh's law. Spherical particles with diameters comparable to the wavelength will scatter according to the Mie theory. Note that experimental investigations show that ensembles of irregularly shaped, but arbitrarily oriented, particles also exhibit scattering which can be satisfactorily described by the Mie theory.

Atmospheric spectral transmissivity profiles show that only two windows (MWIR 3.5 – 5.5 microns and LWIR 8 – 14 microns) are of interest for satellite-borne IR spectropolarimetric imaging systems. Limits may readily be placed on the atmospheric optical thickness in each window. For MWIR wavelengths, at moderate spectral resolution, the optical thickness will lie in the range 0.5 – 1.0; for LWIR wavelengths, it will lie in the range 0.2 – 0.5. Representative MWIR, LWIR wavelengths of 5-10 microns will be adopted to illustrate the functional dependence of atmospheric depolarization effects on wavelength and optical thickness.
Clear sky atmospheric conditions will be assumed so that we need consider only absorption and emission phenomena; scattering of thermal radiation is not significant. Because thermal emission and absorption phenomena are independent of polarization, we can treat natural atmospheric radiation as completely unpolarized. We will adopt a model atmosphere stratified in plane parallel layers and we will suppose the target of interest to be located at sea level.

Depolarization theory for the general situation of propagation of an arbitrarily polarized signal through a non-isothermal atmosphere is developed in Section 5.2. Standard atmospheric

radiative transfer techniques for thermal radiation are used. Predictions for a wide range of model atmospheres, together with the special case of an isothermal atmosphere, are presented in graphical form in Section 5.3. Implications of the results are discussed in Section 5.4.

5.2 Depolarization Theory

To begin our investigation of atmospheric depolarization effects, we must first pick a suitable reference frame for defining the orthogonal components of the beam of radiation. For convenience we will select that plane perpendicular to the ground which contains both the quasi-point target of interest and the imaging spectropolarimeter itself. Vibrations of the electric vectors of the radiation within and perpendicular to this reference plane will be denoted by the subscripts 1, 2 respectively. Later, we will find that selection of the precise orientation of these orthogonal axes within the plane transverse to the direction of propagation may be arbitrary.

If the polarized signal leaving the target in the direction of the sensor is described by these two orthogonal components of the radiance I, given by I_1, and I_2, we have the fundamental relationship that

$$I = I_1 + I_2 \tag{5.1}$$

with the polarized signal reaching the sensor after propagation through the atmosphere described by the corresponding orthogonal components of the radiance J given by J_1, and J_2. Explicitly, we can write

$$J = J_1 + J_2 \tag{5.2}$$

$$J = A + B.I \tag{5.3}$$

where A = Foreground Atmospheric Emission, and B = Atmospheric Attenuation Factor. Since both A, B are determined by natural thermal emission and absorption processes we can write

$$A = A_1 + A_2 \; , \quad A_1 = A_2 \; ; \quad B = B_1 = B_2 \tag{5.4}$$

so that (5.2) can be split and rewritten as

$$J_1 = A_1 + B \cdot I_1 \; , \quad J_2 = A_2 + B \cdot I_2 \; . \tag{5.5}$$

For convenience, all radiances A, I, and J are normalized to that Planck function which corresponds to the monochromatic wavelength and site meteorological temperature of interest. To proceed further we define a *True* Degree of Polarization (P) of the signal as

$$P = \frac{I_1 - I_2}{I_1 + I_2} \tag{5.6}$$

and the *Apparent* Degree of Polarization (Q) of the signal as

$$Q = \frac{J_1 - J_2}{J_1 + J_2} \tag{5.7}$$

We wish to determine the *Depolarization Multiplier* (D) defined by

$$D = \frac{Q}{P} \tag{5.8}$$

Substituting (5.5) into (5.7) and making use of (5.1) and (5.4) we readily obtain

$$Q = \left\{ \frac{I_1 - I_2}{I + (A/B)} \right\} \cdot \tag{5.9}$$

Dividing both sides of (5.9) by I we obtain

$$\frac{Q}{I} = \left\{ \frac{I_1 - I_2}{I_1 + I_2} \right\} \left\{ \frac{1}{I + (A/B)} \right\} \cdot \tag{5.10}$$

Making use of (5.6), (5.8) we can rewrite (5.10) in the form

$$D = \left\{ \frac{I}{I + [A/B]} \right\} \cdot \tag{5.11}$$

Note that the Depolarization Multiplier will always lie in the range $0 \leq D \leq 1$. In general, we can write

$$B = \exp\left[-\frac{\tau_1}{\mu} \right] \tag{5.12}$$

where, $\tau_1 =$ Full Optical Thickness of Atmosphere, $\mu = \cos \theta$ and $\theta =$ Sensor Zenith Angle at Target.

In general, the A–parameter must be computed using the procedures described in Appendix A of this Final Report. But, for the special case of an isothermal atmosphere, the normalized A-parameter is given by

$$A = 1 - \exp\left[-\frac{\tau_1}{\mu} \right] \tag{5.13}$$

So we may obtain the solution for an isothermal atmosphere by substituting (5.12) and (5.13) into (5.11) to obtain

$$D = \cfrac{1}{\left\{1 + \left[\exp\left[\dfrac{\tau_1}{\mu}\right] - 1\right]\right\}}$$

<div align="right">(5.14)</div>

5.2.1 Results

Notice that the Depolarization Multiplier depends not only on the atmospheric opacity in the line of sight between the target and the sensor but also on the normalized intrinsic *total* radiance of the signal leaving the target itself. It does not, however, depend on the chosen orientation of the axes which describing the individual orthogonal components of the beam of radiation. An immediate implication is that **left hand and right hand circularly polarized signals do not suffer differential depolarization through atmospheric propagation.**

Isothermal atmospheric predictions are shown in Figs. 5.1, 5.2, and 5.3. Variation of the *Depolarization Multiplier* with both atmospheric optical thickness (τ) and total radiance of the target signal (I) is depicted for each of three choices for the target acquisition geometry, namely μ equal to 1.0, 0.5, and 0.2 respectively. Model atmospheric predictions are shown for MWIR and LWIR wavelengths respectively, all based on calculations presented in Appendix D.

Fig 5.1 Isothermal Model (Mu=1.0)

11
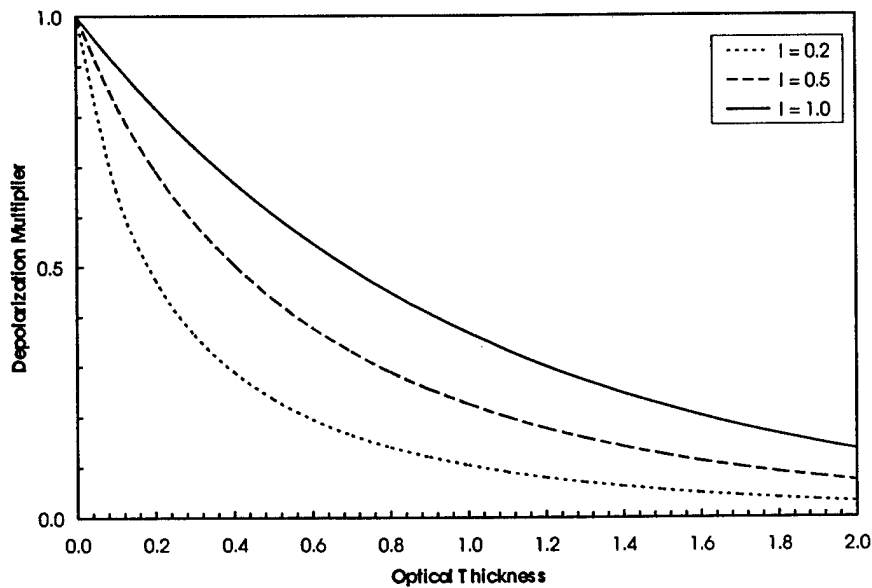
Fig 5.2 Isothermal Model (Mu=0.5)
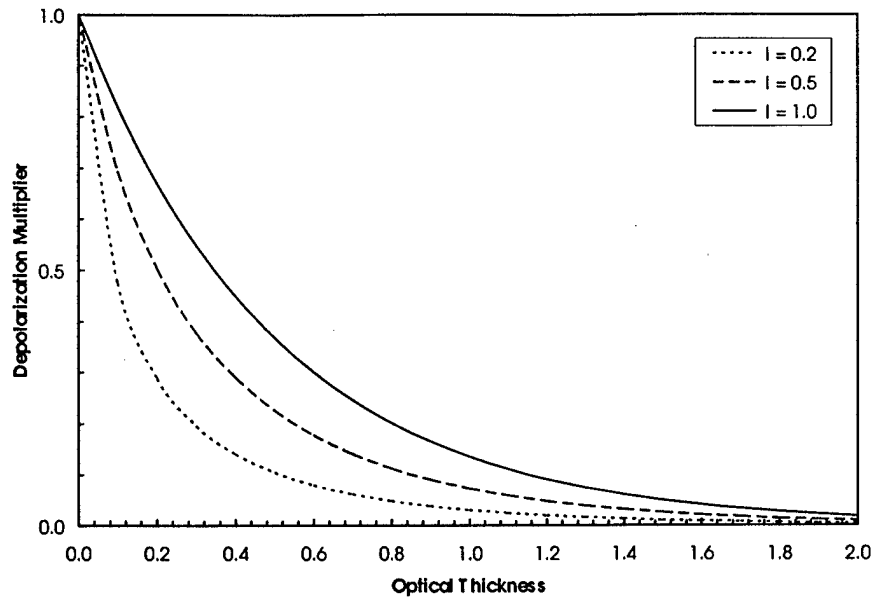
Fig 5.3 Isothermal Model (Mu=0.2)
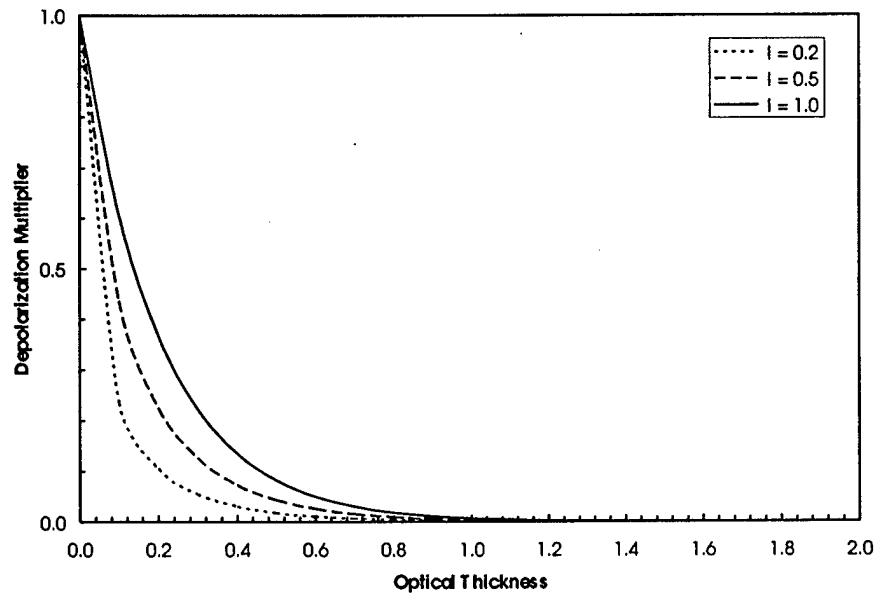
Variation of the *Depolarization Multiplier* with atmospheric optical thickness is shown for a single choice of the total radiance of the target signal, namely unity. Individual figures 5.4 through 5.9 and are presented for each of three choices for the target acquisition geometry, namely μ equal to 1.0, 0.5, and 0.2. Curves labeled "Dry" correspond to the situation where the dominant absorption molecule is *not* water vapor. Curves labeled "Wet" correspond to the situation where water vapor *is* the dominant absorption molecule

12

Fig 5.4 MWIR Mu=1.0
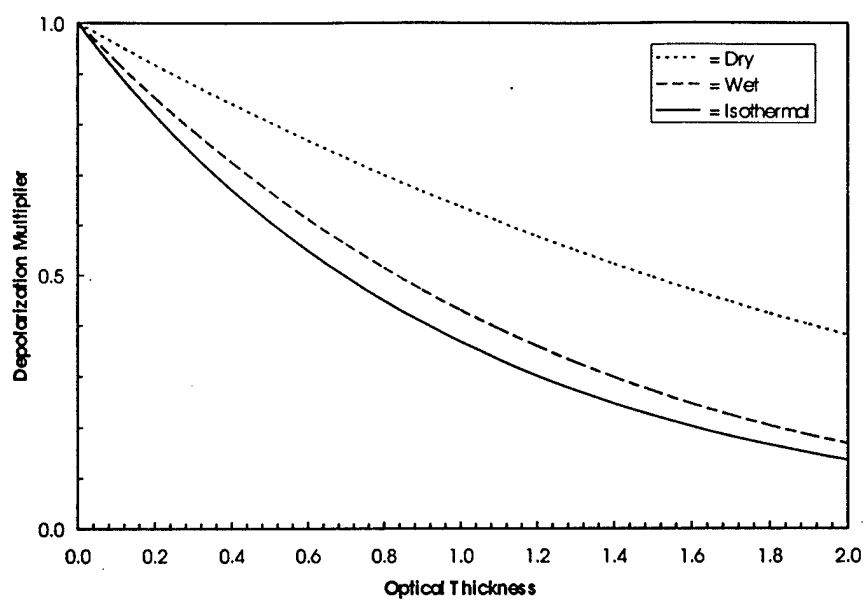
Fig 5.5 MWIR Mu=0.5
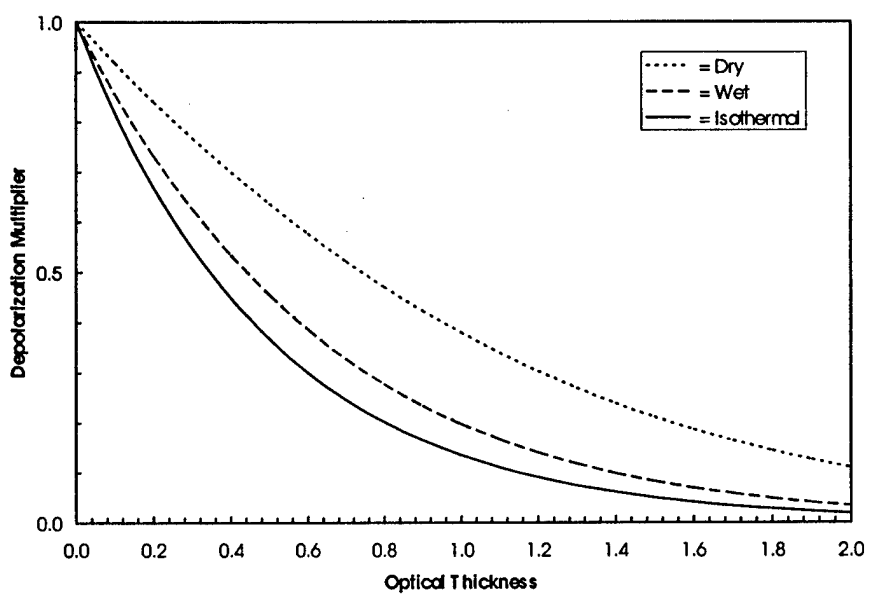
Fig 5.6 MWIR Mu=0.2
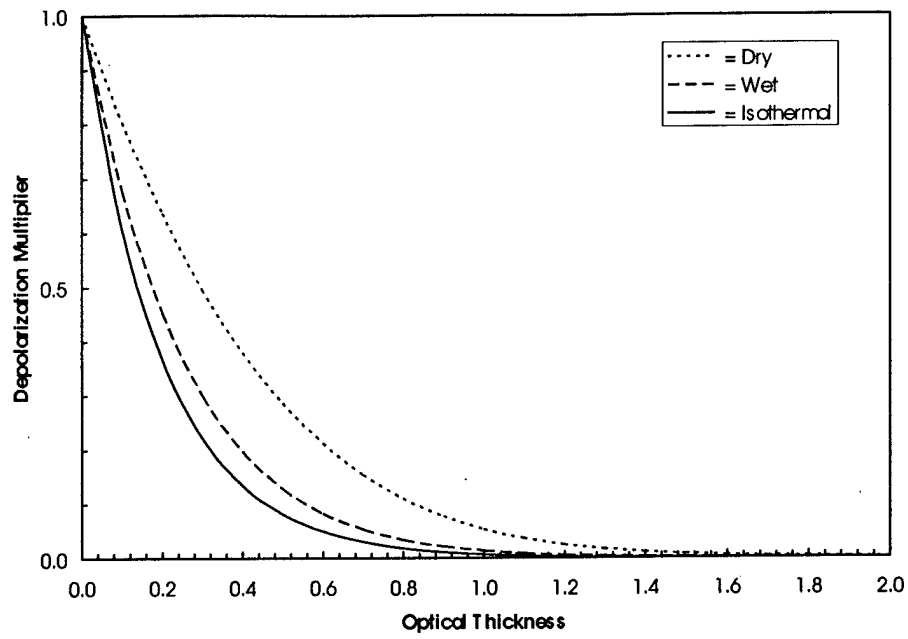
Fig 5.7 LWIR Mu=1.0
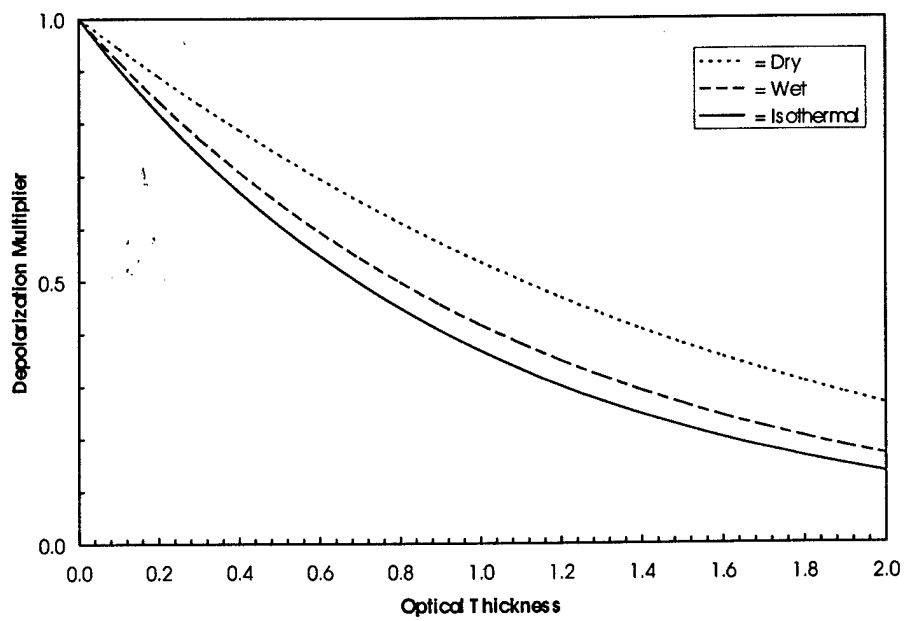
Fig 5.8 LWIR Mu=0.5
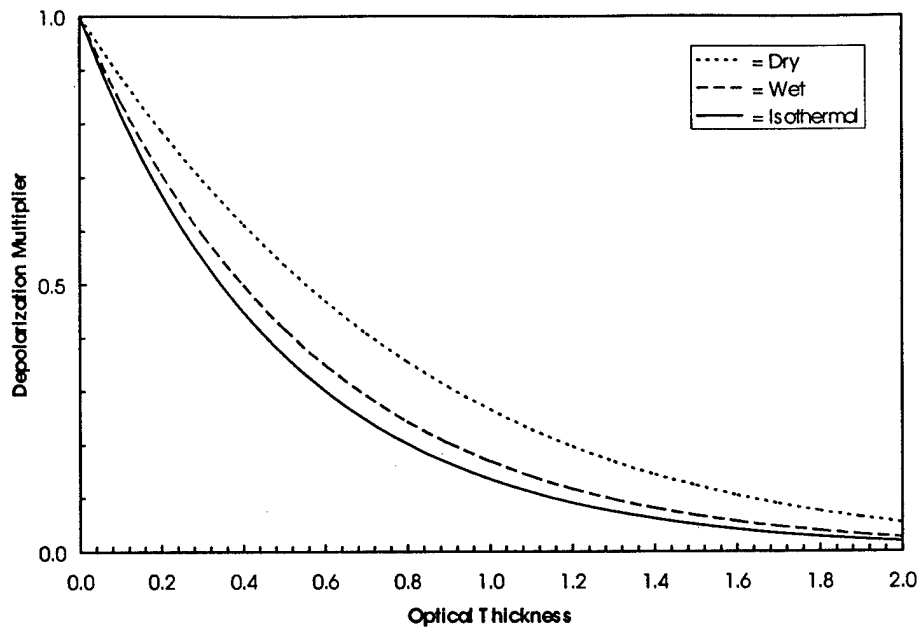
Fig 5.9 LWIR Mu=0.2
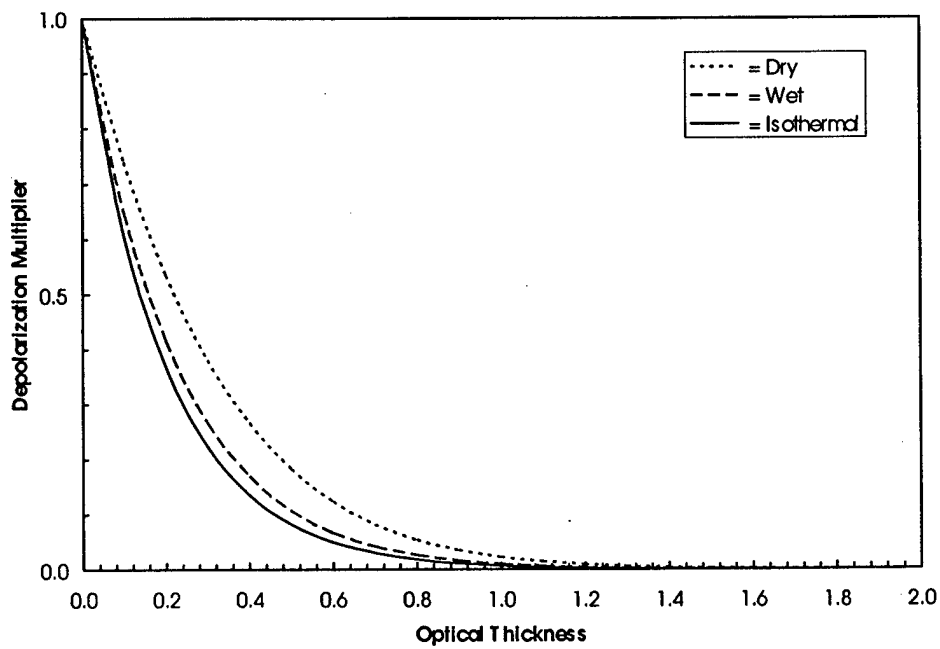
5.2.2 Discussion of Results

Two basic conclusions may be drawn from an examination of the theory.

- Left and right hand circularly polarized signals do not suffer depolarization through atmospheric propagation

- Both linearly and elliptically polarized signals do suffer depolarization through atmospheric propagation

Optimum detection of polarized signals through the atmosphere requires that the Depolarization Multiplier be maximized. Inspection of Figs. 5.1 – 5.9 leads to the following conclusions:

- Depolarization effects are strongly affected by the total radiance of the target itself. Increasing the total signal strength progressively *reduces* the effect of atmospheric depolarization.

- Depolarization effects are strongly affected by the atmospheric opacity. They can range from negligible to catastrophic as the optical thickness changes from very thin to moderately thick.

- Depolarization effects are strongly affected by the total water vapor column abundance within the atmosphere. Less water vapor leads to less depolarization of the target signal. Dry atmospheres are to be preferred.

- Depolarization effects are similar for both the IR wavebands of interest (MWIR, LWIR) when all other parameters are equal.

5.3 Infrared Foreground Emission
5.3.1 Introduction

MWIR (5 μm) and LWIR (10 μm) monochromatic foreground emission radiances versus spacecraft zenith angle are predicted for a sea level site at night. Nine model atmospheres, encompassing the full range of climatic conditions likely to occur at any location and time of year, are employed in this investigation, namely:

- Arctic Winter
- Sub Arctic Winter
- Mid Latitude Winter
- Sub Arctic Summer
- Mid Latitude Summer
- Tropical
- Moist Tropical
- Desert
- 1976 U.S Standard

An isothermal atmosphere at the meteorological air temperature is also used for comparison.

Clear sky atmospheric conditions are assumed so that only absorption and emission need be considered; scattering of thermal radiation is not significant. Since atmospheric absorption &

16

emission effects are usually dominated by either water vapor or non-water-vapor molecules, depending on the precise wavelength selected, both extremes are considered in this parametric study; they are labeled as Dry and Wet respectively.

Our treatment is based on standard radiative transfer techniques and procedures relevant to infrared atmospheric radiation A generalized theory for the case of any non-isothermal atmospheres is first developed. Then predictions are presented in graphical form. For convenience all sky radiances are normalized to the monochromatic Planck function at the meteorological temperature of interest.

5.3.2 Theory

To begin we will define the notation to be used in the analysis. Explicitly, we will model the atmosphere by stratified plane parallel layers. Let

$$\theta = \text{Zenith Angle of Radiance} \quad \mu = \cos\theta$$

$$x = \text{Altitude MSL}$$

$$\sigma = \text{Monochromatic Molecular Absorption Cross-Section}$$

$$P(x) = \text{Monochromatic Planck Function}$$

$$n(x) = \text{Number Density of Absorbing Molecule}$$

$$N(0) = \int_0^\infty n(x)dx = \text{Full Column Density of Absorbing Molecule}$$

$$N(x) = \int_x^\infty n(x)dx = \text{Partial Column Density of Absorbing Molecule}$$

$$\tau = N(x)\sigma = \text{Monochromatic Optical Depth Down To Altitude } x$$

$$\tau_1 = N(0)\sigma = \text{Monochromatic Optical Depth Down To Sea Level} \qquad (5.15)$$

Notice that (5.15) may bee solved for the σ - parameter, once $N(0)$ is known and τ_1 is selected. In essence, we are treating σ as independent of both pressure and temperature throughout the entire vertical profile of the atmosphere. Different σ - parameters apply for the individual situations of Dry and Wet.

For a non-isothermal atmosphere, the foreground emission radiance $I(\mu)$ is given in general by

17

$$I(\mu) = \frac{\sigma}{\mu} \int_0^\infty n(x) P(x) \exp\left\{-\frac{\sigma N(x)}{\mu}\right\} dx \qquad (5.16)$$

so that, normalizing by the Planck function at zero altitude, we obtain

$$\frac{I(\mu)}{P(0)} = \frac{\sigma}{\mu P(0)} \int_0^\infty n(x) P(x) \exp\left\{-\frac{\sigma N(x)}{\mu}\right\} dx \qquad . \qquad (5.17)$$

For the special case of an isothermal atmosphere (5.17) becomes

$$\frac{I(\mu)}{P(0)} = \frac{\sigma}{\mu} \int_0^\infty n(x) \exp\left\{-\frac{\sigma N(x)}{\mu}\right\} dx \qquad (5.18)$$

this may be rewritten as

$$\frac{I(\mu)}{P(0)} = \int_0^\infty \exp\left\{-\frac{\sigma N(x)}{\mu}\right\} \cdot n(x) \sigma \frac{dx}{\mu} \qquad (5.19)$$

or

$$\frac{I(\mu)}{P(0)} = \int_{\tau_1}^0 \exp\left\{-\frac{\tau}{\mu}\right\} \cdot \frac{d\tau}{\mu} \qquad (5.20)$$

this reduces to

$$\frac{I(\mu)}{P(0)} = 1 - \exp\left\{-\frac{\tau_1}{\mu}\right\} \qquad . \qquad (5.21)$$

For large optical thicknesses $\tau_1 \to \infty$ so that

$$\frac{I(\mu)}{P(0)} \to 1, \text{ independent of } \mu \qquad . \qquad (5.22)$$

For small optical thicknesses $\tau_1 \to 0$ so that

$$\frac{I(\mu)}{P(0)} \to \frac{\tau_1}{\mu} \qquad (5.23)$$

or, more explicitly

$$\frac{I(\theta)}{P(0)} \rightarrow \tau_1 . \sec\theta \qquad\qquad (5.24)$$

5.3.3 Predictions

For each waveband and model atmosphere selected optical thicknesses in the range $0 \leq \tau_1 \leq 2$ together with μ values of 0.2, 0.5, and 1.0 were considered. Situations were the dominant absorption molecule is either non-water vapor (Dry) or water vapor itself (Wet) were treated separately. MWIR predictions are illustrated in Figs 5.10 – 5.12; LWIR predictions are illustrated in Figs 5.13 – 5.15. In each graph extreme bounds for the model predictions for both the "dry" and "wet" scenarios are shown together with results for an isothermal atmosphere. In the latter case, the predictions are independent both of the wavelength of the radiation and of the nature of the dominant absorption molecule.

Fig.5.10 MWIR Foreground Emission (Mu=0.2)
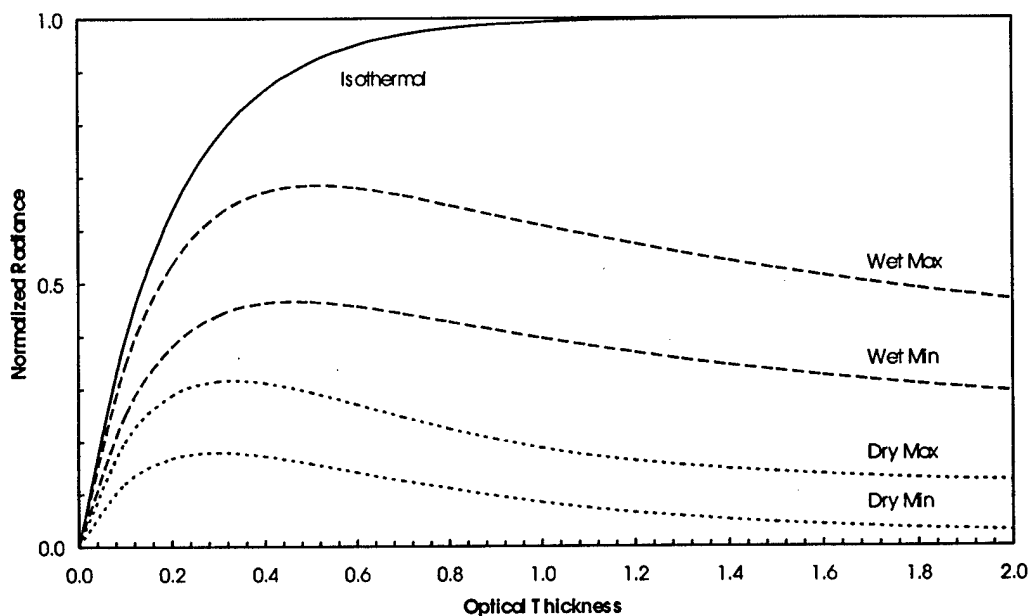
Fig. 5.12 MWIR Foreground Emission (Mu=1.0)
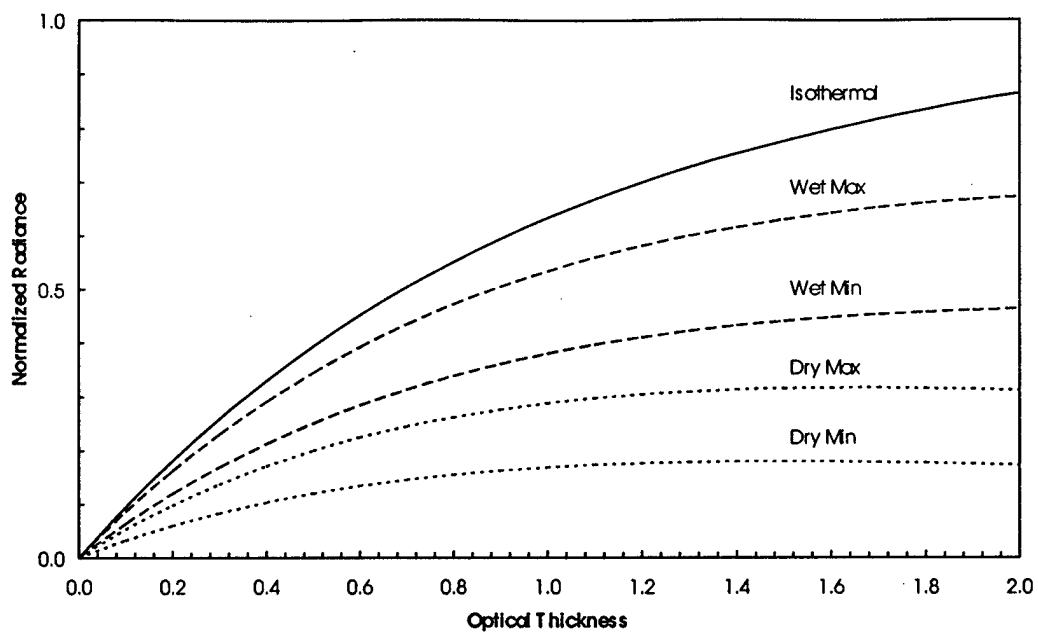
Fig.5.13 LWIR Foreground Emission (Mu=0.2)
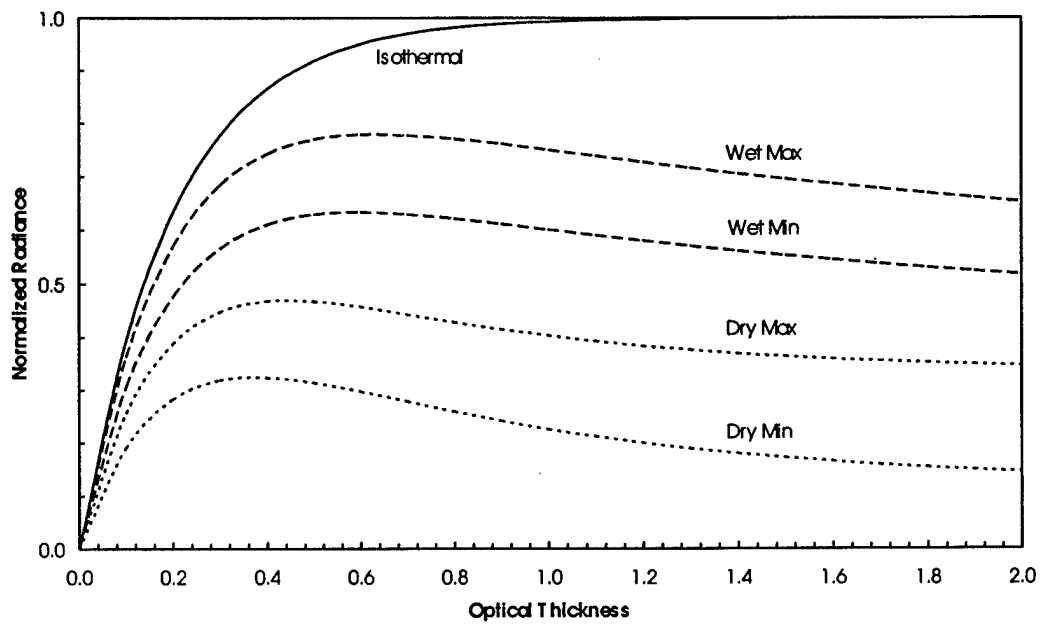
Fig. 5.14 LWIR Foreground Emission (Mu=0.5)

Normalized Radiance vs Optical Thickness. Curves labeled: Isothermal, Wet Max, Wet Min, Dry Max, Dry Min.
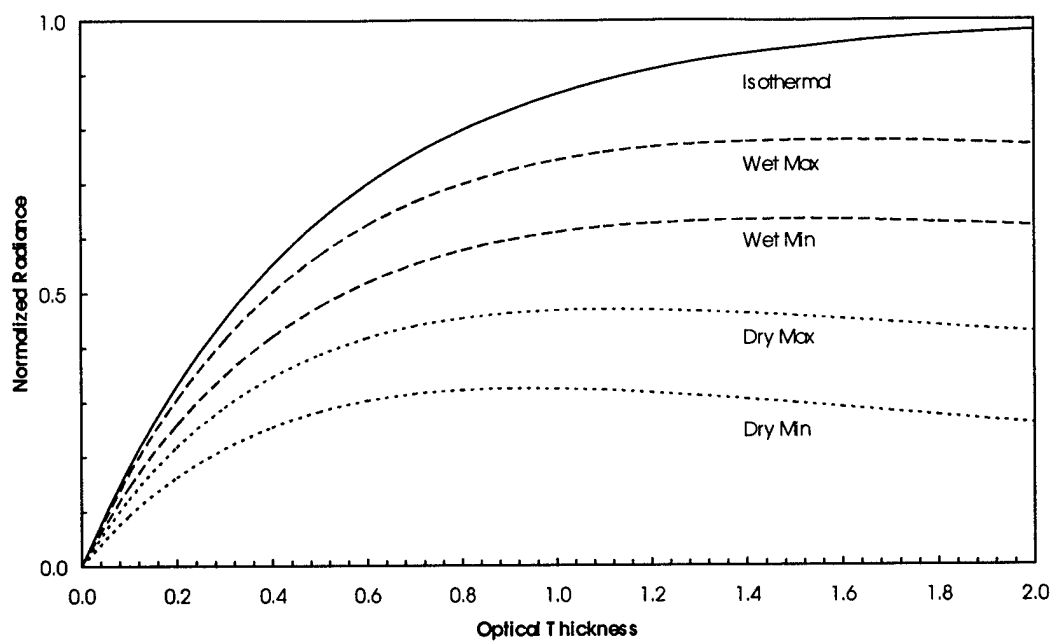
Fig. 5.15 LWIR Foreground Emission (Mu=1.0)

Normalized Radiance vs Optical Thickness. Curves labeled: Isothermal, Wet Max, Wet Min, Dry Max, Dry Min.

21
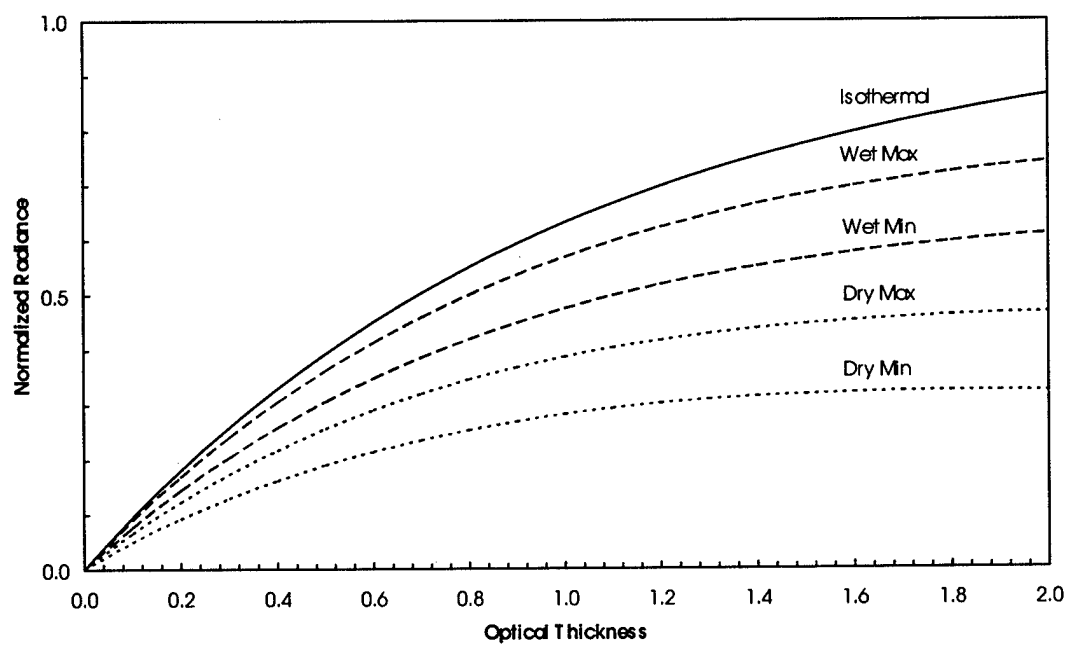
5.4 Equivalent Horizontal Path Lengths Through the Atmosphere

Our theoretical predictions of the depolarization of infrared radiation through atmospheric propagation may be tested by studying laser propagation along horizontal paths. In concept a retro-reflection experiment might be set up between two mountains in the southwest region of the United States. Either Arizona or New Mexico would be ideal because of their prevailing clear atmospheric conditions. In this Technical Memorandum we use simple theory to estimate the magnitude of the required path lengths of interest. Our theoretical analysis will be based on well-known concepts. We will begin by supposing the atmosphere to be isothermal.

We wish to relate the normal optical thickness of the atmosphere (τ) to the equivalent horizontal optical thickness (ξ). Several definitions follow, namely x = Altitude MSL of Horizontal Path; L(x)= Equivalent Horizontal Path Length for Unit Air Mass; H = Scale Height of Dominant IR Absorption Molecule; σ = Cross-Section of Dominant IR Absorption Molecule; N(x) = Number Density of Dominant IR Absorption Molecule

We can write

$$\tau = N(0)H\sigma \tag{5.25}$$

and

$$\xi = N(x)L(x)\sigma \tag{5.26}$$

with the condition

$$\tau = \xi \tag{5.27}$$

we obtain

$$L(x) = \frac{N(0)H}{N(x)} \qquad . \tag{5.28}$$

But

$$N(x) = N(0)\exp\left(-\frac{x}{H}\right) \tag{5.29}$$

so that

$$L(x) = H \exp\left(\frac{x}{H}\right) \tag{5.30}$$

5.4.1 Discussion

If the dominant IR absorption molecule is *not* water vapor we can adopt a scale height ~ 8 km; if water vapor *is* dominant we will adopt a scale height ~ 2 km. These distinct situations will be referred to as Dry and Wet respectively. We are interested in altitudes in the range $0 \leq x \leq 3$ km. Figure 5.16 illustrates the dependence of the Equivalent Path Length on altitude for each situation.

Fig. 5.16 Equivalent Horizontal Path Lengths
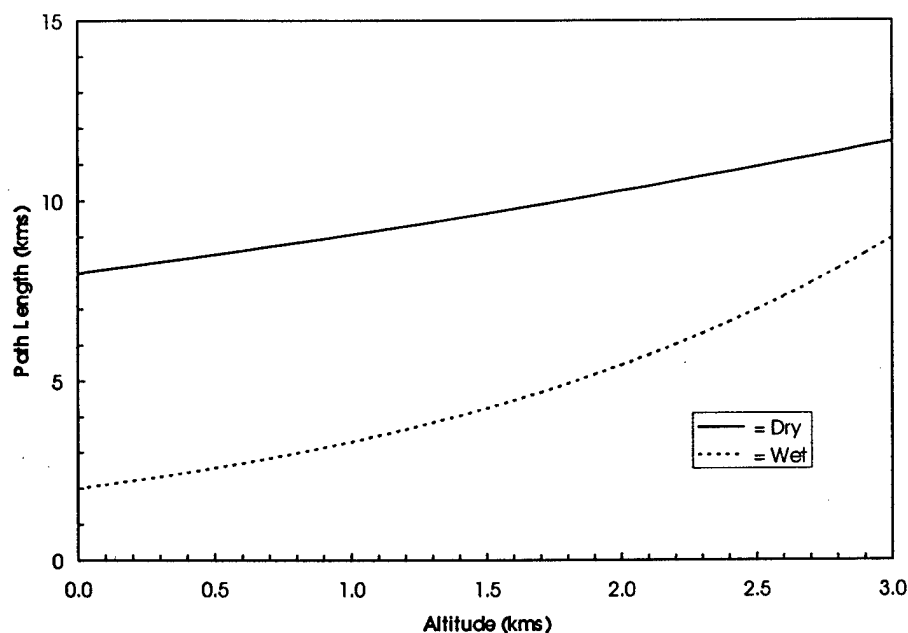
6.0 Infrared Sky Brightness

6.1 Introduction

MWIR (5 μm) and LWIR (10 μm) monochromatic sky radiances versus zenith angle for an isothermal atmosphere are predicted for a sea level site at night. Clear sky atmospheric conditions are assumed so that only absorption and emission need be considered; scattering of thermal radiation is not significant. Atmospheric absorption / emission effects are usually dominated by either water vapor or non-water-vapor molecules depending on the wavelength selected. Both extremes, labeled Wet and Dry respectively, are considered in developing the theory. To demonstrate the functional dependence of sky radiance on wavelength, optical thickness, and zenith angle a generalized theory for an arbitrary atmosphere is developed. Predictions for the special case of an isothermal atmosphere are presented in graphical. For convenience all sky radiances are normalized to the monochromatic Planck function at the meteorological temperature of interest. Recently obtained MWIR wide-band empirical data are reviewed and implications of the results are discussed.

6.2 Theory

Our treatment is based on standard radiative transfer techniques and procedures relevant to infrared atmospheric radiation We will begin by defining the notation to be used in the analysis. Explicitly, we will model the atmosphere by stratified plane parallel layers. Let

$$\theta = \text{Zenith Angle of Radiance} \quad \mu = \cos\theta \tag{6.1}$$

$$x = \text{Altitude MSL} \tag{6.2}$$

$$\sigma = \text{Monochromatic Molecular Absorption Cross-Section} \tag{6.3}$$

$$P(x) = \text{Monochromatic Planck Function} \tag{6.4}$$

$$n(x) = \text{Number Density of Absorbing Molecule} \tag{6.5}$$

$$N(0) = \int_0^\infty n(x)\,dx = \text{Full Column Density of Absorbing Molecule} \tag{6.6}$$

$$N(x) = \int_x^\infty n(x)\,dx = \text{Partial Column Density of Absorbing Molecule} \tag{6.7}$$

$$\tau = N(x)\sigma = \text{Monochromatic Optical Depth Down To Altitude } x \tag{6.8}$$

$$\tau_1 = N(0)\sigma = \text{Monochromatic Optical Depth Down To Sea Level} \tag{6.9}$$

Notice that (6.9) may be solved for the σ - parameter, once N (0) is known and τ_1 is selected. In essence, we are treating σ as independent of both pressure and temperature throughout the entire vertical profile of the atmosphere.

In general, for a non-isothermal atmosphere, the sky radiance I (μ) is given by

$$I(\mu) = \frac{\sigma}{\mu} \int_0^\infty n(x)P(x)\exp\left\{-\frac{\sigma[N(0)-N(x)]}{\mu}\right\} dx \tag{6.10}$$

so that, normalizing by the Planck function at zero altitude, we obtain

24

$$\frac{I(\mu)}{P(0)} = \frac{\sigma}{\mu} \int_0^\infty n(x) \frac{P(x)}{P(0)} \exp\left\{-\frac{\sigma[N(0)-N(x)]}{\mu}\right\} dx \qquad . \qquad (6.11)$$

For the special case of an isothermal atmosphere (6.11) becomes

$$\frac{I(\mu)}{P(0)} = \frac{\sigma}{\mu} \int_0^\infty n(x) \exp\left\{-\frac{\sigma[N(0)-N(x)]}{\mu}\right\} dx \qquad (6.12)$$

this may be rewritten as

$$\frac{I(\mu)}{P(0)} = \int_0^\infty \exp\left\{-\frac{\sigma N(0)}{\mu}\right\} . \exp\left\{\frac{\sigma N(x)}{\mu}\right\} . n(x)\sigma\frac{dx}{\mu} \qquad (6.13)$$

or

$$\frac{I(\mu)}{P(0)} = \exp\left\{-\frac{\sigma N(0)}{\mu}\right\} \int_0^\infty \exp\left\{\frac{\sigma N(x)}{\mu}\right\} . n(x)\sigma\frac{dx}{\mu} \qquad (6.14)$$

or

$$\frac{I(\mu)}{P(0)} = \exp\left\{-\frac{\tau_1}{\mu}\right\} \int_0^{\tau_1} \exp\left\{\frac{\tau}{\mu}\right\} . \frac{d\tau}{\mu} \qquad (6.15)$$

this reduces to

$$\frac{I(\mu)}{P(0)} = 1 - \exp\left\{-\frac{\tau_1}{\mu}\right\} \qquad . \qquad (6.16)$$

For large optical thicknesses $\tau_1 \to \infty$ so that

$$\frac{I(\mu)}{P(0)} \to 1...independent...of \ \mu \qquad . \qquad (6.17)$$

For small optical thicknesses $\tau_1 \to 0$ so that

$$\frac{I(\mu)}{P(0)} \to \frac{\tau_1}{\mu} \qquad (6.18)$$

or, more explicitly

$$\frac{I(\theta)}{P(0)} \to \tau_1.sec\theta \qquad . \qquad (6.19)$$

6.3 Predictions

To illustrate the basic morphology of the sky radiance graphics, we will make predictions for an isothermal atmosphere. Note that, in this scenario only, the predictions are independent both of the wavelength of the radiation and of the nature of the dominant absorption molecule. Atmospheric optical thicknesses in the range $0 \leq \tau_1 \leq 2$ together with μ values in the range $0 \leq \mu \leq 1$ are considered. The results are summarized in Figs. 6.1, 6.2, and 6.3.

Fig. 6.1 Sky Radiance: Isothermal
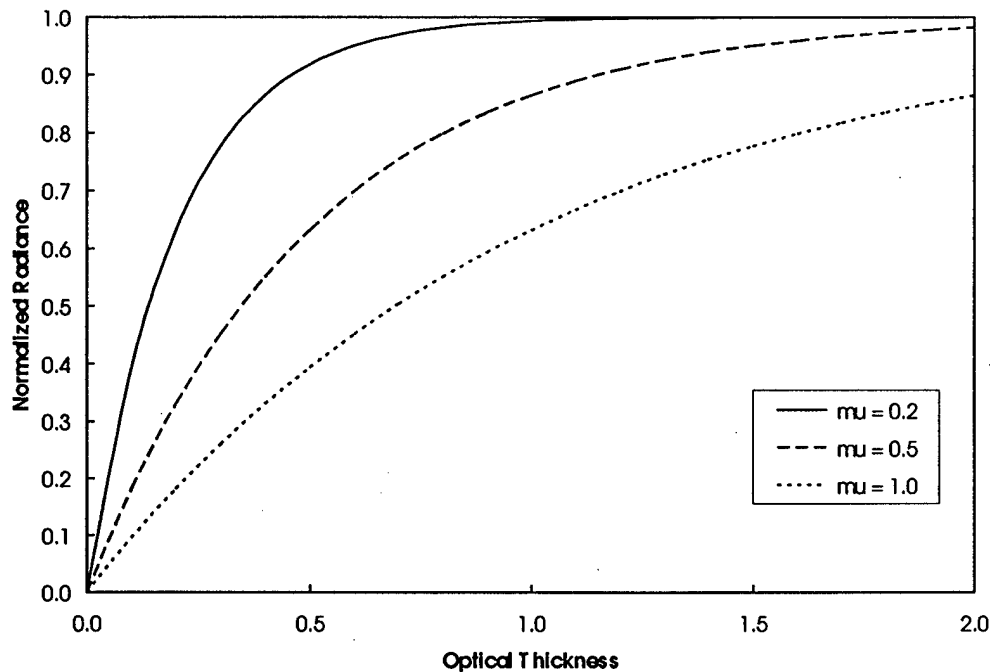
6.4 Empirical Data

MWIR waveband-integrated sky radiance measurements have been made for two U.S. sites, S (Sea Level) and M (7500 feet MSL) using a Minard SA-10 radiometer. Multiple azimuth scans were made at zenith angles ranging from zero to near 90°. Sky radiance measurements (I) were found to be symmetric in azimuth but to vary linearly with the secant of the zenith angle (θ), at least up to θ equals 72°. Empirically, we have

$$I(\theta) = A + B \sec\theta \qquad (6.20)$$

where A, B are constants for the particular site / atmosphere / radiometer chosen. Observation and theory are in remarkably good morphological agreement considering the simplicity of the model.

26

Origin of the linear relation lies in the existence of both optically thick and optically thin spectral regions within the integrated MWIR waveband. In the center of the 3-5 micron waveband lies the optically thick 4.4 micron CO_2 absorption feature. Spectral windows on either side are optically thin with their opacities influenced by water vapor band absorption. In fact, variation in the water vapor emission was found to be very largely responsible for the variation of sky radiance with zenith angle at the different sites at different times.

6.5 Discussion
Careful inspection of the theory shows that use of an isothermal atmosphere overestimates the sky brightness radiance compared with the actual situation where the atmospheric temperature decreases with altitude. Precise predictions should therefore be based on more representative model atmospheres.

7.0 Modeling the Infrared Radiation Scattering Properties of Cirrus Clouds

7.1 Introduction
We begin with a review of the physical structure of cirri form clouds and continue with a discussion of the manner in which radiation is scattered by ice crystals. Our fundamental approach to solving the radiative transfer problem is described in Section 4. It is based on two related ideas. A highly anisotropic scattering problem is reduced to one involving only isotropic scattering. The hexagonal ice crystals involved are replaced by equivalent ice spheres, Existing radiative transfer similarity rules are used to modify both the single scattering albedo and the optical thickness of the layer of ice crystals as required. The optical properties of equivalent ice spheres are then reviewed. Radiative transfer parameters suitable for investigating the propagation of polarized IR radiation through cirrus clouds are discussed and chosen in. Appendix A describes the scattering phase function of the individual ice crystals.

7.2 Physical Structure of Cirrus Clouds
Cirri form clouds are classified into three broad types, namely cirrus (ci), cirrostratus (cs), and cirrocumulus (cc). Cirrus, which is found at the greatest altitudes, has a fibrous structure that is threadlike in appearance and is often composed of detached elements that are arranged in the sky in an irregular manner. Cirrostratus is composed of thin whitish sheets of clouds that resemble a fibrous veil covering the entire sky. Cirrocumulus usually consists of regular arrays of small white flakes of cloud that develop from cirrostratus. All three of these basic types are found to exist in a variety of forms, with a host of names used to describe their shape, color, and structure. Cirri form clouds are generally restricted to the altitude range 20-40 thousand feet; they are most often found in the range 25-30 thousand feet. Their vertical thickness can range from negligible to 15-20 thousand feet; the most frequent thickness is 5-6 thousand feet. Water content of cirri form clouds is typically on the order of 0.01 gr m^{-3}. Cirri form clouds are composed exclusively of ice crystals in the form of hexagonal columns. By studying photographs of ice crystals collected in cirrus clouds Jacobowitz, [1970] obtained information with respect to the size and form of the crystals. Typical cirrus crystals have major axes that range in length from 100 to 300μm, with a mean value of about 150μm, and minor axes that range in length from 40 to 100μm, with a mean value of about 60μm.

Deductions from visual optical phenomena and laboratory studies of falling bodies which simulate ice crystals falling in air lead to the conclusion that the ice crystals are randomly oriented in any horizontal plane in the cloud but are not random in all three dimensions. Usually, but not always, the crystals tend to be oriented with their long axes randomly distributed within the horizontal plane. Although Hall, [1968] provides some evidence that the axes of the prisms or plates are oriented at random, the existence of pronounced optical effects suggests that at least on occasions preferential orientation of the crystals occurs, with one of their axes being predominantly vertical.

7.3 Scattering of Radiation by Ice Crystals

Computations performed for the actual crystal shapes by Jacobowitz, [1970; 1971], Coleman, [1979], and Wendling et. al., [1979] have successfully reproduced the major observed optical phenomena, including the 22°and 46° halos. These authors also found that the scattering pattern is insensitive to variation in crystal size in the range likely to be encountered in cirrus clouds. For the infrared wavelength range he studied (11-15μm) and the sizes of the crystals involved, Jacobowitz, [1971] concluded that refraction through the crystals is negligible and that the scattering patterns could be well approximated by Kirchoff diffraction and surface reflection.

Jacobowitz [1970] further showed that if the ice crystals were approximated by circular cylinders and if they were randomly oriented (either in a plane or in three dimensions) their diffraction patterns would be nearly identical to those for spheres, which scatter the same total amount of energy. Earlier, van de Hulst, [1957] had considered scattering by infinite cylinders of circular cross-section and found that they behave similarly to spherical particles of the same radius. Both van de Hulst [1957] and Wendling et. al., [1979] found that column-like crystals randomly oriented in a plane behave rather like spherical particles and not like columns randomly oriented in space. Coleman, [1979] presented a complete solution to the radiation scattered by finite hexagonal ice crystals based on geometric ray tracing. Although his solution is restricted to scatterers, which are much larger than the incident wavelength, it is general in all other respects, such as scattering with and without absorption and scattering by plates and columns. The solution yields information on the scattered energy for the perpendicular and parallel Fresnel components of the scattered rays and on the linear polarization of the scattered radiation. Earlier Ockmann, [1958] had indicated that although hexagonal ice is birefringent the difference in the optical characteristics for the two directions of polarization was not great.

Within the infrared region of the spectrum Coleman, [1979] predicted diffraction patterns, scattering phase functions, and linear polarization for finite hexagonal ice crystals. He used a two-dimensional (2D) scattering model, with the crystals described by their radius (R) / length (L) ratio. For 10.6μm radiation, linear polarization calculations were made for crystals described by columns (R/L equal to 1/5) and plates (R/L equal to 5/1). For precise forward scattering, corresponding to a scattering angle (Θ) equal to zero, linear polarization is typically less than ± 5 percent. For the range $30 \leq \Theta \leq 150°$, linear polarization is positive; it passes through a maximum of ~ 60 percent for $\Theta \sim 90°$.

7.4 Reduction to Isotropic Scattering

In essence, scattering of radiation by ice crystals may be conveniently divided into three separate parts. One part is the sharply peaked pattern around the forward direction that is due to diffraction; the second is the radiation reflected from the surface; and the third is due to

refraction within the crystals. For ice crystals that are randomly oriented in space, the pattern due to diffraction can be well approximated by the pattern derived for equivalent spheres. When the wavelength of radiation in the Earth's atmosphere is not very large compared with the dimensions of the scattering centers - the case in point for the MWIR / LWIR wavebands - the radiative transfer problem presents formidable computational difficulties. Rigorous solutions must be obtained from the equation of transfer with an appropriate scattering phase function and source term. But, because of the complicated form or nature of this phase function, standard methods for the solution of the equation of transfer are frequently impracticable and one must resort to approximate methods.

That situation is exactly the case in point. Approximate radiative transfer methods generally utilize no more than three parameters to describe the scattering properties of the medium; they are the single scattering albedo, the asymmetry factor of the individual scattering phase function, and the optical thickness of the medium. The latter is dependent upon the extinction cross-section of the scattering particles. More significantly, when the atmosphere is vertically inhomogeneous, the radiative transfer problem must be reduced to one involving only isotropic scattering (i.e., two parameters only) if results are to be obtained rapidly using typical workstation equipment. Fortunately, specialized methods involving 'similarity relationships' have been developed to achieve this reduction. Our approach follows that of Goody and Yung, [1989]. Reducing the radiative transfer problem in cirrus clouds to one of isotropic scattering begins with a consideration of the forward scattering peak. We will start by defining the notation to be used. Specifically, we set the individual particle parameters as

$$a = \text{single scattering albedo}$$
$$e = \text{extinction cross-section}$$
$$k = \text{absorption cross-section}$$
$$s = \text{scattering cross-section}$$

with the τ - symbol adopted for the optical thickness of the scattering medium. Making use of these definitions, we can write:

$$a = \frac{s}{k+s} \tag{7.1}$$

and

$$e = k + s \quad . \tag{7.2}$$

Let us compare two scattering media, characterized by the parameter sets (a, k, s, e, τ) and $(a_0, k_0, s_0, e_0, \tau_0)$. The former has a fraction, b, of the scattered energy concentrated in a narrow forward peak, while the latter has no such singular behavior. But, the absorption process is independent of the scattering, so that

$$k_0 = k \quad . \tag{7.3}$$

But, since scattering into the forward peak is equivalent to no scattering at all, the two sets of parameters must be related by

$$s_0 = s(1-b) \qquad \cdot \qquad (7.4)$$

It follows that the extinction parameters are related by

$$e_0 = e(1-ab) \qquad (7.5)$$

and the single scattering albedos by

$$a_0 = a\,(1-b)/(1-ab) \qquad (7.6)$$

Furthermore, since optical thickness is directly proportional to the extinction cross-section, we must have

$$\frac{\tau_0}{\tau} = \frac{e_0}{e} \qquad (7.7)$$

this reduces to

$$\tau_0 = \tau(1-ab) \qquad \cdot \qquad (7.8)$$

Our problem is therefore reduced to one of isotropic scattering, once the fundamental parameters a, b are known. In keeping with the particular approach of this section, we will approximate the individual scattering phase function of ice particles $\Phi(\alpha)$ by isotropic scattering with a forward peak. In Appendix A we define $\Phi(\alpha)$ in terms of a series of Legendre polynomials, we provide a definition of the asymmetry parameter (g), and we discuss normalization of the function. Following van de Hulst, [1980], we can write

$$\Phi(\alpha) = 1 - g + 2g\delta(1-\cos\alpha) \qquad (7.9)$$

where α is the angle of scattering, and the forward peak is described by a delta-function (δ).
It is a simple matter to show that the fraction of energy scattered into the backward hemisphere is (1-g)/2. It follows that the fraction of scattered energy within the forward peak (b) is equal to the asymmetry parameter (g). Knowledge of both the single scattering albedo (a) and the asymmetry parameter (g) for equivalent ice spheres is summarized below.

7.5 Optical Properties of Equivalent Spheres

Irvine and Pollack, [1968] have critically reviewed the literature on the wavelength dependent absorption and reflection properties of ice. Quantitative descriptive information was summarized by them in tabulated parameters (k_λ, c_λ), together with information on both the real and complex parts of the refractive index (n_r, n_i). Mie theory was used to compute the single scattering albedo (a), the asymmetry parameter (g), and the normalized extinction cross section for spheres of ice with radii 0.3, 1.0, 3.0, and 10.0 microns throughout the wavelength range $0.7 \leq \lambda \leq 200$ microns.

Irvine and Pollack, [1968] were able to find a simple, but reliable, generalized formula for the calculation of the a - parameter for situations in which $x \geq 2$ (where x equals $2\pi.r / \lambda$, and r equals particle radius with λ equal to the wavelength of the radiation). If we represent the cirrus particles as equivalent spheres of radius 60μm, the x - condition / requirement is met for both the MWIR and LWIR regions of the spectrum. Over the MWIR atmospheric window the mean

value of the single scattering albedo (a) was computed to be 0.5146 ± 0.0150. They also found a general asymptotic behavior where a →0.5 as k_λ. r →infinity, where k_λ is the absorption parameter. For the MWIR (3.5μm – 5.5μm) window, k_λ varies through the range 270 – 921 cm^{-1}; for the LWIR (8μm – 14μm) window the corresponding k_λ range is 250 – 1260 cm^{-1}. Comparing the k_λ. r product values across MWIR and LWIR wavebands, we can expect the LWIR single scattering albedo (a) to lie in the range $0.5 \le a \le 0.5146$. In view of uncertainties in the empirical formula used for these calculations, we will simply adopt a single scattering albedo (a) of 0.5 for both the MWIR and LWIR atmospheric windows.

Selection of a suitable value for the asymmetry parameter (g) may be carried out by considering the work of van de Hulst, [1980]. He showed that the g-parameter increases with increasing radius for non-absorbing spheres. He also provided limiting values for two choices of n_r. For n_r equal to 1.333, 1.5 the corresponding g values are 0.884, 0.83 respectively. For weak (or partially) absorbing spheres, we can expect the value of g to rise slightly because the diffraction peak and the grazing reflection assume relatively more prominence than radiation refracted in the sphere itself. But, for strongly absorbing spheres, exhibiting metallic scattering properties, the value of g drops below that for non-absorbing spheres since radiation is no longer refracted within and through the particle. On the basis of van de Hulst's analysis, together with the results obtained by Irvine and Pollack, we will adopt an asymmetry parameter g equal to 0.881 for ice particles in cirrus clouds, for both the MWIR and LWIR atmospheric windows.

Modification of the single scattering albedo (a) and optical thickness (τ) of a layer of ice crystals for use in the equivalent radiative transfer problem involving isotropic scattering may be carried out by the procedures given in Section 4. Explicitly, for an equal to 0.5 and g equal to 0.881, we obtain the reduced single scattering albedo (a_0) equal to 0.1 and the reduced optical thickness ($τ_0$) equal to 0.6τ.

7.6 Discussion
IR radiation propagating through a layer of cirrus cloud should become depolarized in the same manner as we found to occur for clear atmospheres. The depolarization theory developed in Appendix I of this Report is directly applicable if the calculation of the foreground emission and the total optical thickness in the line of sight are suitably modified. Close to the forward scattering direction any linear polarization will be negligible. Primary scattering should dominate over multiple scattering since the cloud layer will be optically thin for those operational situations of interest. Multiple scattering, if it should become significant due to increasing cloud thickness, would have the effect of depolarizing incident radiation. Ambient atmospheric thermal radiation scattered by the ice particles should remain essentially unpolarized due to the natural polydispersions of the crystal sizes and to their probable quasi-random orientations.

31

In summary, therefore, we will adopt the following sets of cirrus model parameters:

Physical Structure:
Lower and upper boundaries of the cirri form cloud layer are at altitudes of
      8 km and 10 km MSL respectively
Within the cirri form layer the mixing ratio (ice particles-to-gas molecules
      is uniform both vertically and horizontally

Infrared Radiation Scattering
All scattered radiation is completely depolarized
Individual ice particles scatter isotropically
Each ice particle has an equivalent single scattering albedo equal to 0.1
The *equivalent* optical thickness of a layer of ice particles is 0.6 times the *actual* value
Scattering parameters are constant throughout the spectral range 3 – 14μm

One final comment, infrared laboratory reflectance measurements of ice, for near-normal angles of incidence and reflection, made by Schaaf and Williams [1973], show that the reflectivity is very low (0.01 – 0.06) throughout the spectral range 3 – 14μm at the meteorologically interesting temperature of -7 degrees C. In essence, therefore, we can consider the cirrus particles to be very nearly perfectly absorbent throughout the atmospheric spectral windows of interest.

8.0 Application of Scattering Theory to the Transport of Polarized LWIR Signals
8.1 Introduction
In prior Sections, the transport of polarized LWIR signal is studied on the assumption that the terrestrial atmosphere continuous fluid. In Section 8, these results are compared with results from small sphere scattering theory. Figure 8-1 shows the scattering geometry used in the Section.
A train of plane waves with wavelength λ are incident on a smooth uniform sphere of radius of a and an index of refraction n. Due to the symmetry of the scattering geometry and conservation of momentum the angular dependence of the scattered wave on depends on the angle θ between the incident and outgoing Poynting Flux vectors (blue arrows).

8.2 Atmospheric Attenuation
In 1910, Einstein used the theory of plane wave scattering by small sphere to study the scattering and attenuation of light through gases. The resulting Einstein-Smoluchowski formula is given by (8-1 & 8-2)

$$I(x) = I_0 e^{-\alpha x} \tag{8-1}$$

$$\alpha = \frac{1}{6N\pi} \left(\frac{\omega}{c}\right)^4 \left| \frac{(n_R^2 - 1)(n_R^2 + 2)}{3} \right|^2 N k_B T \beta_T \tag{8-2}$$

where,
I is intensity and I_0 is the intensity at x = 0
x is propagation distance

α is the attenuation or extinction coefficient in dB

N is the number of particles in a unit volume

ω is the angular frequency of the wave, $\omega = 2\pi c/\lambda$

c is the speed of light

n_R is the real part of the index of refraction

k_B is Boltzman's constant

T is temperature in degrees Kelvin

β_T is the isothermal compressibility
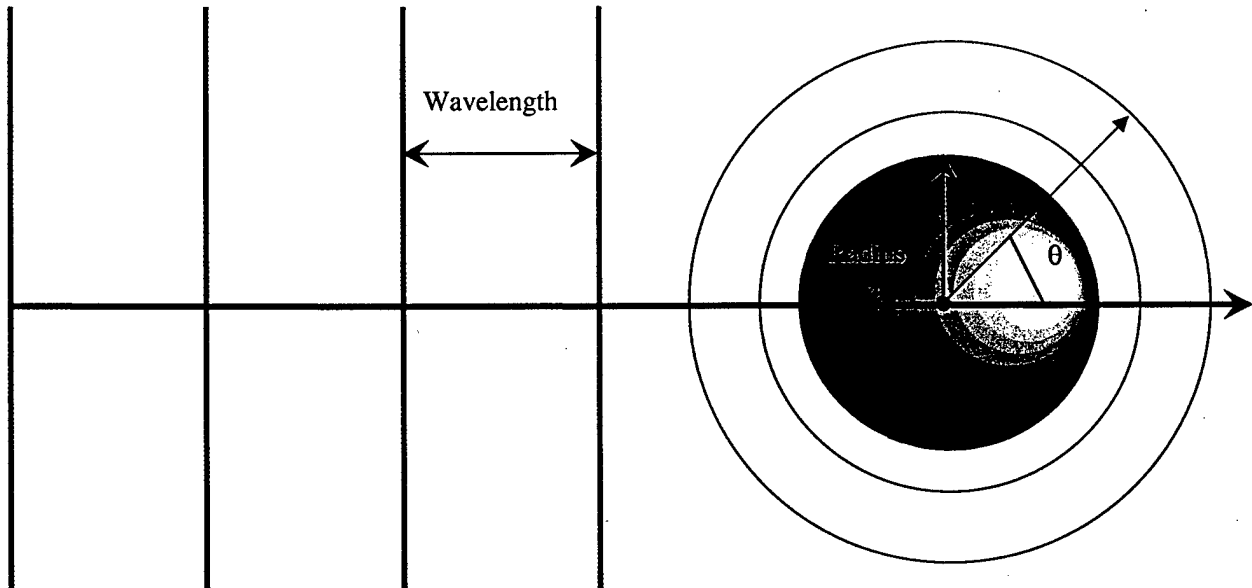
Figure 8-1 The plane wave scattering by small sphere -geometry.
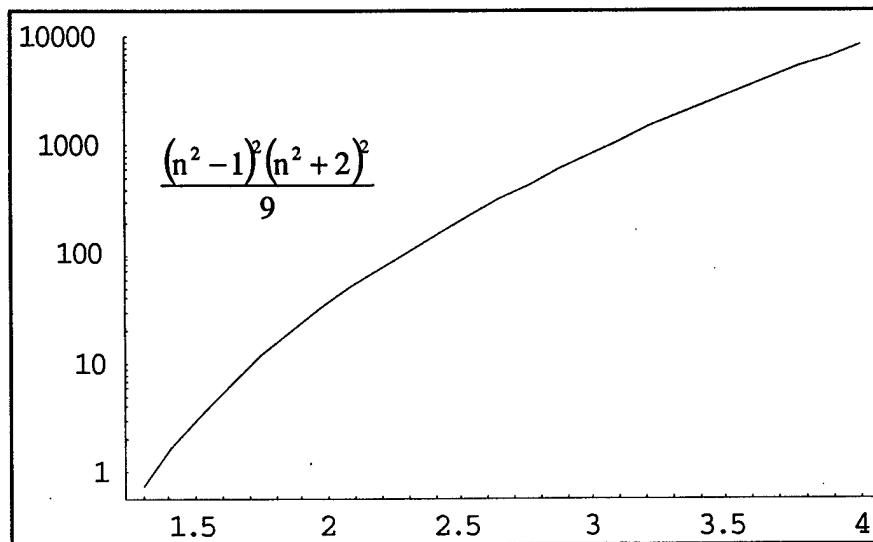
Figure 8.2.The value of the term in absolute value brackets in (8.2) as a function of n.

For a dilute idea gas, with $n_R^2 \ll 1$ and $N\, k_B\, T\, \beta_T = 1$ (8.2) reduces to Rayleigh's [1871] scattering

$$\alpha = \frac{32\pi^3}{3N\lambda^4}(n_R - 1)^2 \qquad (8\text{-}3)$$

Substituting (8-2) into (8-1) shows that longer wavelength light suffer less attenuation in the atmosphere then short wavelength light, as first pointed out by Rayleigh in his proof of why the sky color is blue and at sunset and sun raise the sun appears red.

If the correlation length, Λ of atmospheric density fluctuations increase the value of β_T becomes very large and approaches infinity at point of critical opalescence. For large values of Λ the value of α becomes anisotropic and is given by (8-4)

$$\frac{d\alpha(\theta)}{d\Omega} = \frac{3}{16\pi}\left(1 + Cos^2\theta\right)\alpha\left[\frac{1 + \Lambda^2 q^2 / N k_B T \beta_T}{1 + \Lambda^2 q^2}\right] \qquad (8\text{-}4)$$

where,

$$q^2 = 2(\omega/c)^2 (1 - Cos^2\theta) \text{ and the value of } \alpha \text{ is given by (8-2)}$$

For $\Lambda q \ll 1$ (8.4), integration over the normalized angular distribution gives back (8.2). However, for $\Lambda \to \infty$ the angular integration of (8.4) is proportional to $(c/\Lambda\omega)^2 Ln(\Lambda\omega/c)\,\alpha$. Near the critical point of $\Lambda \to \infty$, the frequency dependence of α becomes $1/\lambda^2$ instead of the usual $1/\lambda^4$ Rayleigh wavelength dependence.

8.3 Mie Scattering
8.3.1 Scattering Cross Sections
The general problem of the scattering of electromagnetic waves by smooth sphere of arbitrary optical properties and when $2\pi a/\lambda$ is not small was solved by [Mie,1908] and [Debye,1909] for cylinders, and are also presented in all versions of Born and Wolf. The infinite series solutions for $I_\perp(\theta)$ and $I_\parallel(\theta)$ and the Mathematic™ code for calculating them are given in Appendix D

The relevant results from Mie Scattering theory are summarized below, where σ, the cross section, is the power scattered per particle (or molecule) for a unit incident energy flux, and the fractional loss of flux through a distance dx in the gas is $N\sigma dx$. Equations (8.5) – (8.9) are for dielectric spheres, and (8.10) – (8.14) are for perfectly conduction spheres, and are given by Jackson, [1999], where ε_R is the real part of the dielectric constant of the particle and $\varepsilon_R = |n|^2$.

$$\frac{d\sigma_\parallel}{d\Omega} = 8\pi^4 a^2 (a/\lambda)^4 \left|\frac{\varepsilon_R - 1}{\varepsilon_R + 2}\right|^2 Cos^2\theta \qquad (8.5)$$

$$\frac{d\sigma_\perp}{d\Omega} = 8\pi^4 a^2 \left(a/\lambda\right)^4 \left|\frac{\varepsilon_R - 1}{\varepsilon_R + 2}\right|^2 \tag{8.6}$$

$$\Pi(\theta) = \frac{\dfrac{d\sigma_\perp}{d\Omega} - \dfrac{d\sigma_\parallel}{d\Omega}}{\dfrac{d\sigma_\perp}{d\Omega} + \dfrac{d\sigma_\parallel}{d\Omega}} = \frac{Sin^2\theta}{1 + Cos^2\theta} \tag{8.7}$$

$$\frac{d\sigma}{d\Omega} = \frac{d\sigma_\perp}{d\Omega} + \frac{d\sigma_\parallel}{d\Omega} = 8\pi^4 a^2 \left(a/\lambda\right)^4 \left|\frac{\varepsilon_R - 1}{\varepsilon_R + 2}\right|^2 \left(1 + Cos^2\theta\right) \tag{8.8}$$

$$\sigma = \int \frac{d\sigma}{d\Omega} d\Omega = \frac{128}{3}\pi^5 a^2 \left(a/\lambda\right)^4 \left|\frac{\varepsilon_R - 1}{\varepsilon_R + 2}\right|^2 \tag{8.9}$$

$$\frac{d\sigma_\parallel}{d\Omega} = 8\pi^4 a^2 \left(a/\lambda\right)^4 \left|Cos\theta - \tfrac{1}{2}\right|^2 \tag{8.10}$$

$$\frac{d\sigma_\perp}{d\Omega} = 8\pi^4 a^2 \left(a/\lambda\right)^4 \left|1 - \tfrac{1}{2}Cos\theta\right|^2 \tag{8.11}$$

$$\frac{d\sigma}{d\Omega} = 16\pi^4 a^2 \left(a/\lambda\right)^4 \left[\tfrac{5}{8}\left(1 + Cos^2\theta\right) - Cos\theta\right] \tag{8.12}$$

$$\Pi(\theta) = \frac{3Sin^2\theta}{5\left(1 + Cos^2\theta\right) - 8Cos\theta} \tag{8.13}$$
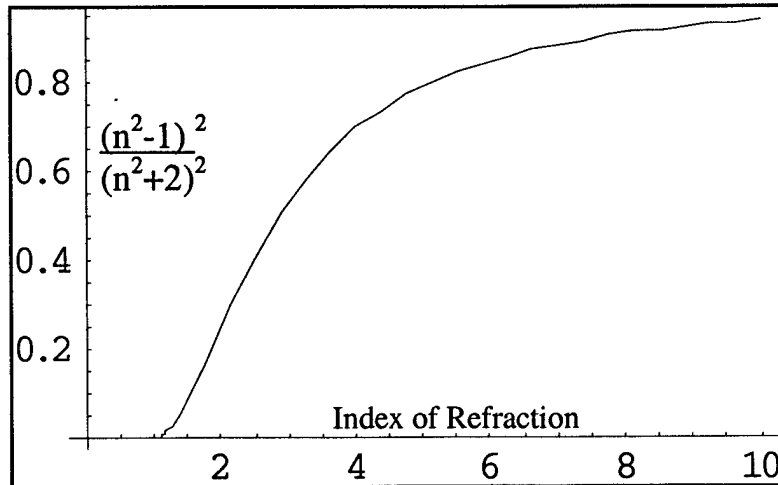
Figure 8.3.Value of the term brackets in (8.5-8.6) and (8.8-8.9) as a function of n

35
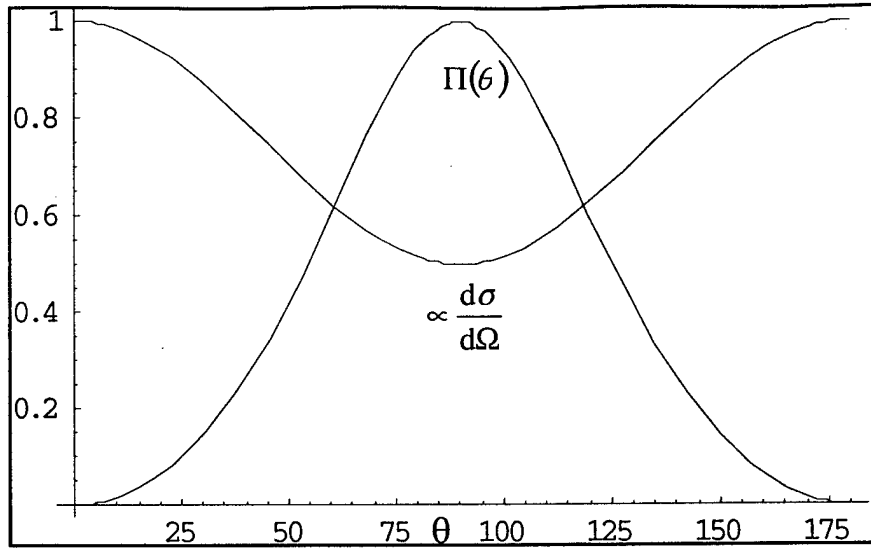
Figure 8.4.The polarization anisotropy amplitude, Π and total differential scattering cross section for dielectric spheres as a function of scattering angel θ.
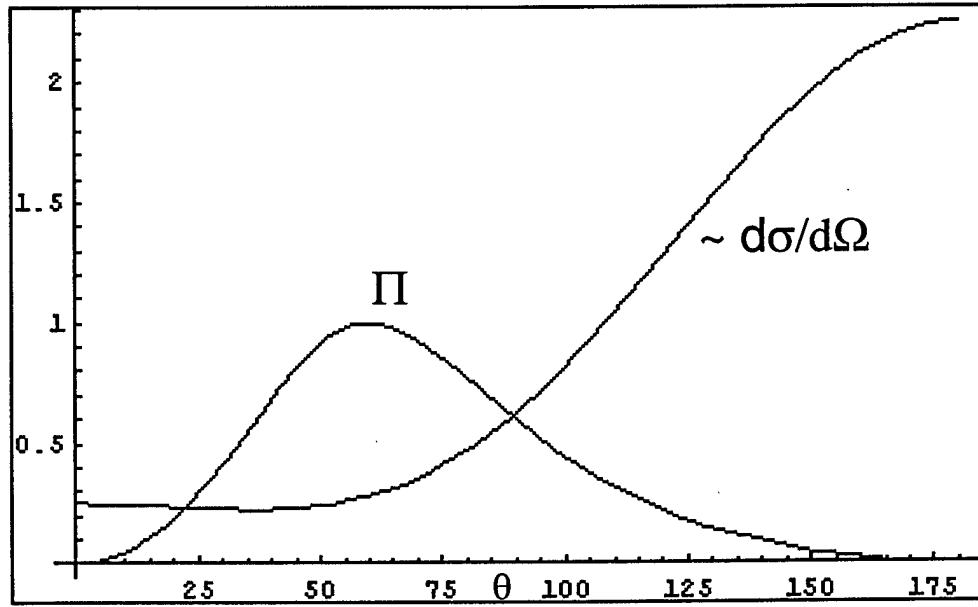
Figure 8.5.The polarization anisotropy amplitude, Π and total differential scattering cross section for perfectly conducting spheres as a function of scattering angel θ.

Equation (8.14) gives the total differential scattering cross section for elliptically or circularly polarized light

$$\frac{d\sigma}{d\Omega} = 16\pi^4 a^2 (a/\lambda)^4 \left[\tfrac{5}{8}\left(1 + Cos^2\theta\right) - Cos\theta - \tfrac{3}{4}\left(\frac{r}{1+r^2}\right) Sin^2\theta\, Cos(2\phi - \alpha) \right] \qquad (8.14)$$

36

where, r =0 for left-hand polarized light, r = ∞ for right-hand polarized light, ϕ is the angle of polarization and α is given by (8.2).
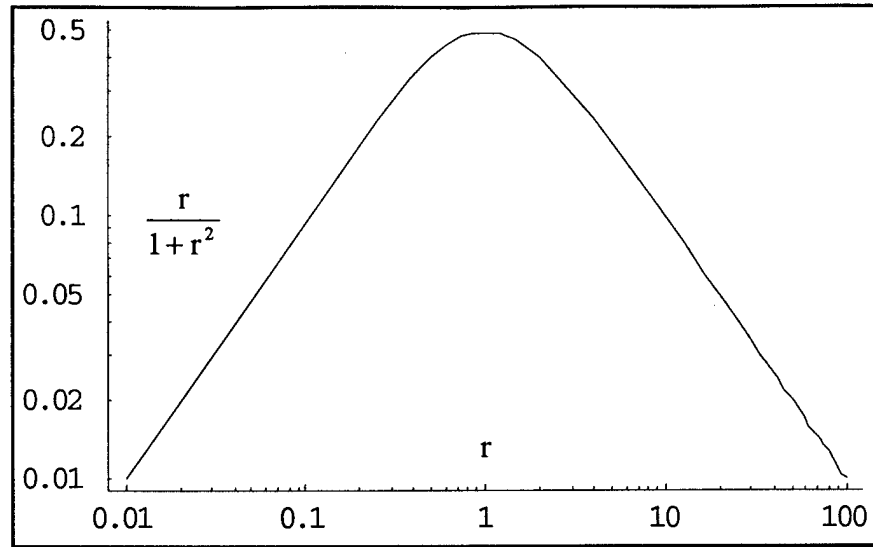
Figure 8.6.The value of the r/(1+r²) term in (8.14) as a function of the polarization factor r.

Equation (8.14) shows **that the differential scattering cross section is the same for left-hand and right-hand circularly polarized light** and is given by (8.15). This result is same as that found by the different analysis used in prior Sections of this report.

$$\frac{d\sigma}{d\Omega} = 16\pi^4 a^2 (a/\lambda)^4 \left[\tfrac{5}{8}\left(1+\text{Cos}^2\theta\right) - \text{Cos}\theta\right] \qquad (8.15)$$
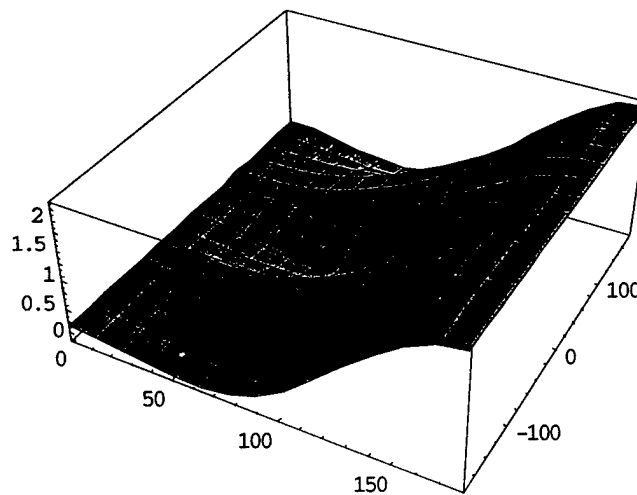
Figure 8.7 The angular dependence of (8.16) as a function of the scatter angle $0^0 \le \theta \le 180^0$ and polarization angle $-100^0 \le \phi \le 100^0$.

Equation (8.16) gives the total differential scattering cross section for linearly polarized light

$$\frac{d\sigma}{d\Omega} = 16\pi^4 a^2 (a/\lambda)^4 \left[\tfrac{5}{8}(1+Cos^2\theta) - Cos\theta - \tfrac{3}{8}Sin^2\theta\, Cos2\phi\right] \tag{8.16}$$

Equation (8.16) shows **that the differential scattering cross section is not the same for parallel and perpendicularly linearly polarized light.** This result is the same as also that found by the different analysis used in prior Sections of this report. Equation (8.16) reduces to (8.17) for the case of parallel ($\phi = 0^0$) linearly polarized light and (8.18) for the case of perpendicularly
($\phi = 90^0$) linearly polarized light.

$$\frac{d\sigma_\parallel}{d\Omega} = 16\pi^4 a^2 (a/\lambda)^4 \left[\tfrac{5}{8}(1+Cos^2\theta) - Cos\theta - \tfrac{3}{8}Sin^2\theta\right] \tag{8.17}$$

$$\frac{d\sigma_\perp}{d\Omega} = 16\pi^4 a^2 (a/\lambda)^4 \left[\tfrac{5}{8}(1+Cos^2\theta) - Cos\theta + \tfrac{3}{8}Sin^2\theta\right] \tag{8.18}$$

The polarization amplitude Π for this case is identical to (8.13)

8.3.2 Variable Dependencies

We used the shareware application MiePlot v2.0.1 [http://www.philiplaven.com] to study in detail how Mie scattering solutions depend of the value of the variables, a, λ, and n. The accuracy of the MiePlot results were checked using the Mathematica™ v4.2 code shown in Appendix M. Because MiePlot only plots to a monitor it is necessary to use the "Print Screen" keyboard command to capture MiePlot results. This has the advantage that the value range of values for all the variables of the problem are also captured and attached to the intensity plots.

38

Intensity scale
- Logarithmic
- Linear

Maximum
[Automatic ▼]

Minimum
[Automatic ▼]

Light source
- Point - Sun

Angle scale
Minimum angle
[0]

Maximum angle
[180]

Angular resolution
[0.1 ▼]

Drop size
Radius (µm)
[.5]

- Monodisperse
- Disperse

Light
Number of
wavelengths [1 ▼]

Wavelength (µm) in vacuo
[10] I.R.

Refractive index
Real   Imaginary
[1 5444279] [0]

Polarisation
[Both ▼]

[Mie scattering ▼]

[Intensity v. scattering angle ▼]

Restore defaults
Information ON

——— Perpendicular polarisation   ——— Parallel polarisation

0.001
10^{-4}
10^{-5}
10^{-6}
10^{-7}
10^{-8}
10^{-9}
10^{-10}
10^{-11}
10^{-12}
10^{-13}

0   30   60   90   120   150   180
Scattering angle (degrees)

Figure 8.8 Intensity as a function of scattering angle for $\lambda/a = 20$ and n = 1.544

A comparison of Figs 8.9 – 8.12 clearly shows how the number of oscillations in the Intensity Vs scattering angle plots significantly increases as the value λ/a decreases from 20 to 0.1. These oscillations predicted by Mie theory are in very good agreement with observations [Born and Wolf, 2002]
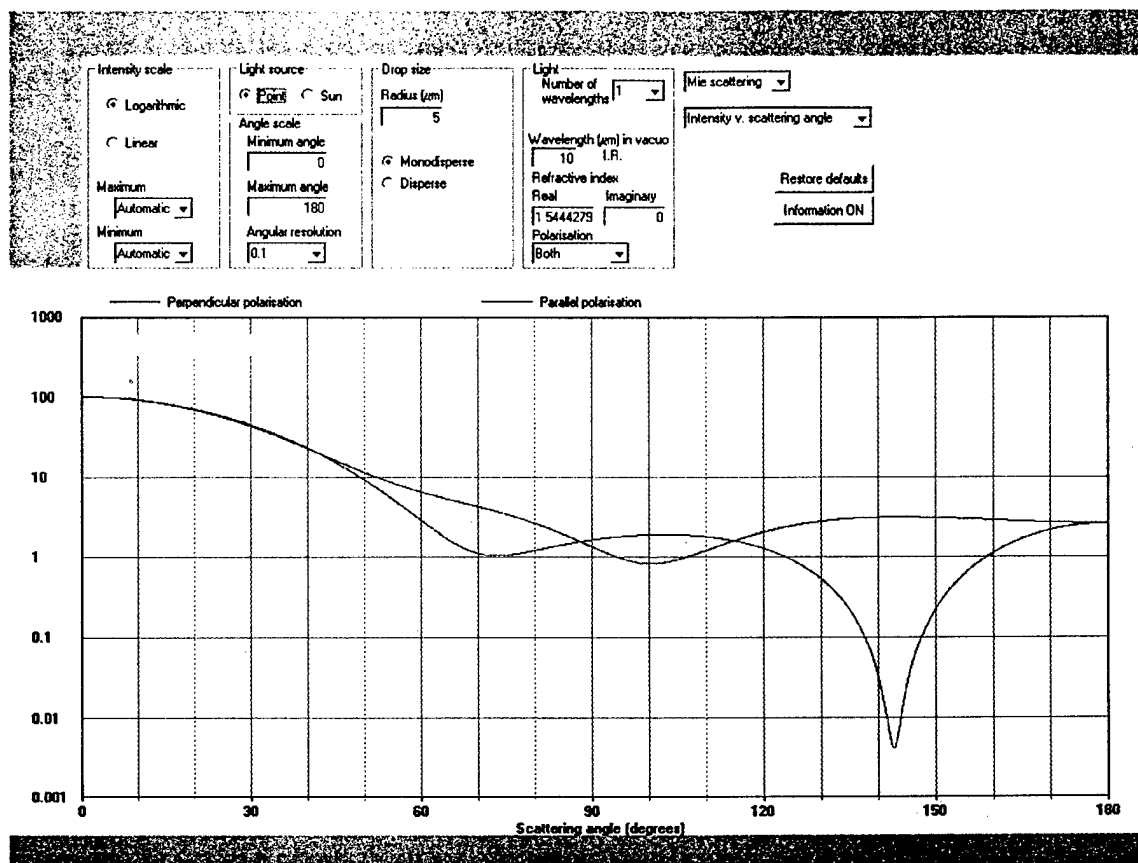
Figure 8.9 Intensity as a function of scattering angle for $\lambda/a = 2$ and $n = 1.544$
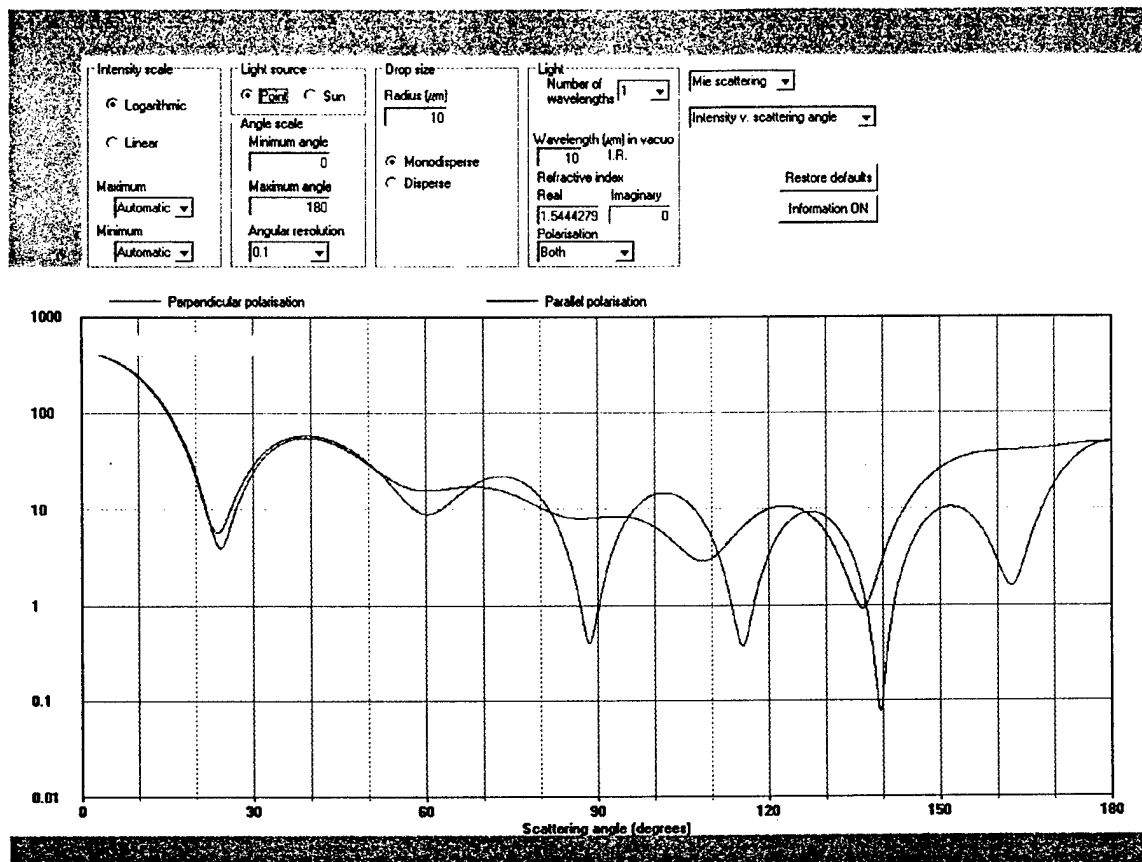
Figure 8.10 Intensity as a function of scattering angle for $\lambda/a = 1$ and $n = 1.544$
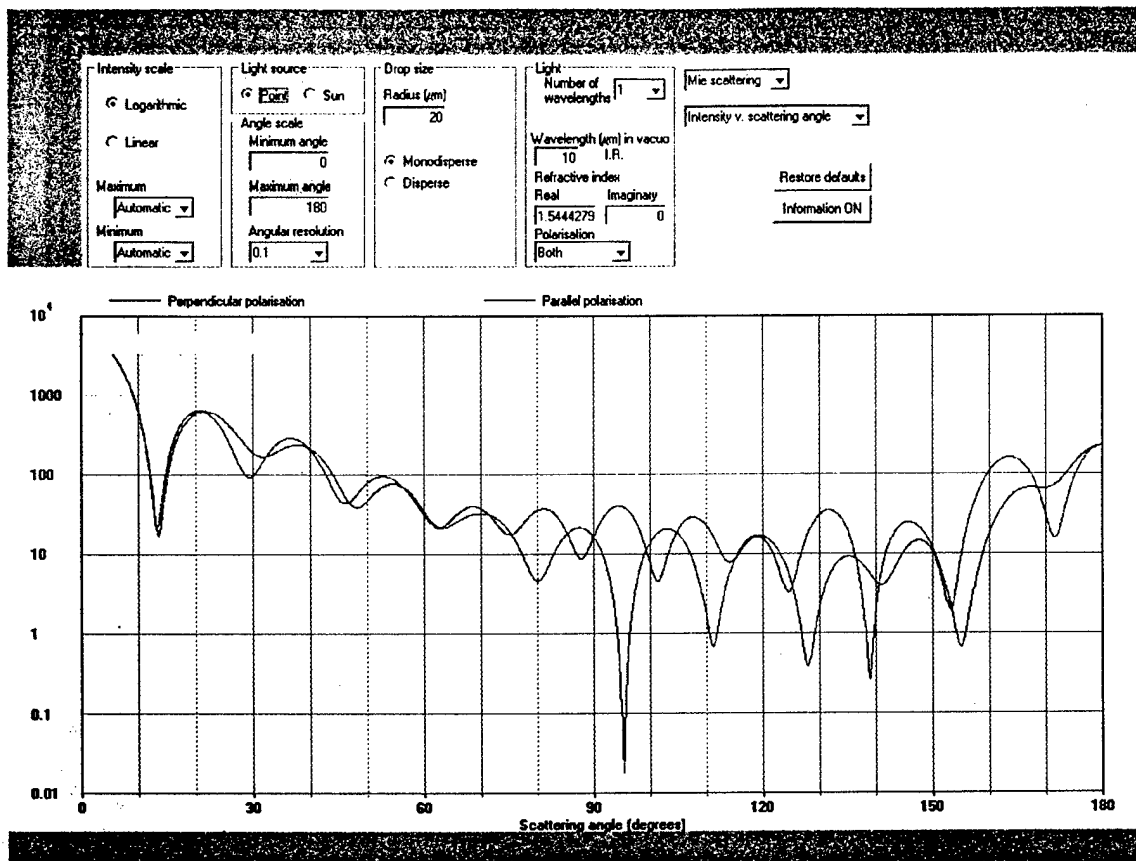
Figure 8.11 Intensity as a function of scattering angle for $\lambda/a = 0.5$ and n = 1.544
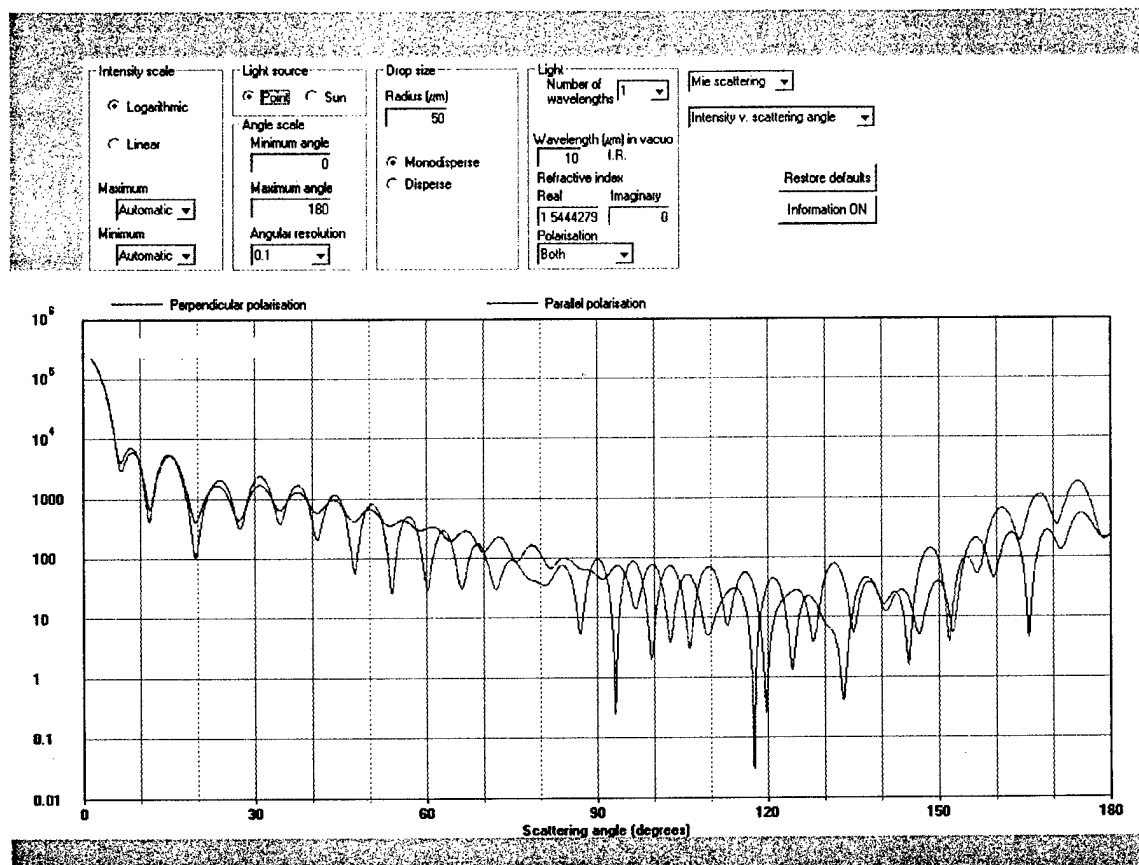
Figure 8.12 Intensity as a function of scattering angle for λ/a = 0.2 and n = 1.544

Perpendicular polarisation   Parallel polarisation
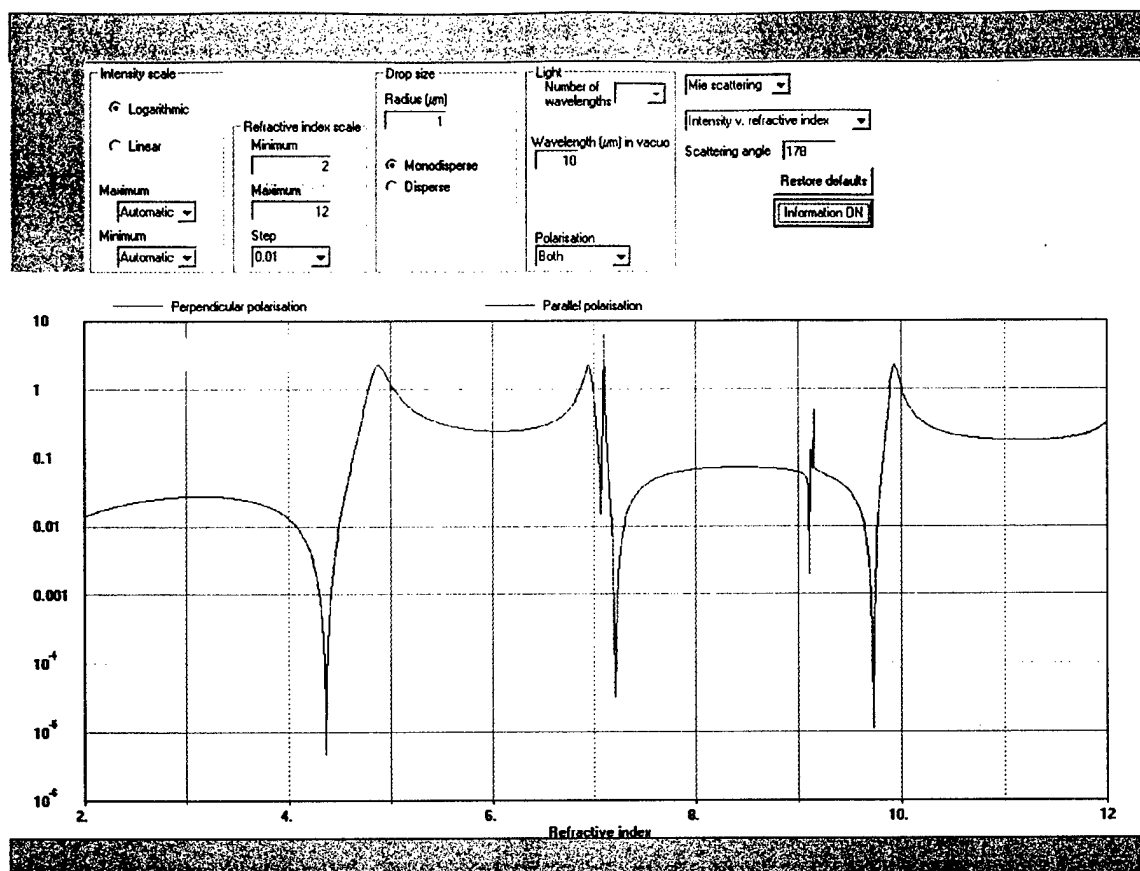
Refractive index

Figure 8.13 Intensity as a function of index of refraction for $\lambda/a = 10$ and $\theta = 178^0$

Figs 8.13 – 8.15 show how the intensity of light scattered backwards, sideways and forward depends on the index of refraction of spheres with $\lambda/a = 10$. Notice the narrow "absorption and emission" features in the intensity are most apparent in Fig. 8-13. We were unable to ascertain the reason for this feature, and suspect in is due to a resonance phenomena. Also note that the only significant polarization anisotropy occurs for sideway scattered light (Fig. 8.14).

Intensity scale

○ Logarithmic

○ Linear

Refractive index scale
Minimum
| 1.5

Maximum
| Automatic ▼ |

Minimum
| Automatic ▼ |

Maximum
| 10 |

Step
| 0.01 ▼ |

Drop size

Radius (μm)
| 1 |

○ Monodisperse
○ Disperse

Light
Number of wavelengths | 1 ▼ |

Wavelength (μm) in vacuo
| 10 |

Polarisation
| Both ▼ |

Mie scattering ▼

Intensity v. refractive index ▼

Scattering angle | 90 |

Restore defaults

Information ON

Perpendicular polarisation   Parallel polarisation

Refractive index

Figure 8.14 Intensity as a function of index of refraction for $\lambda/a = 10$ and $\theta = 90^0$
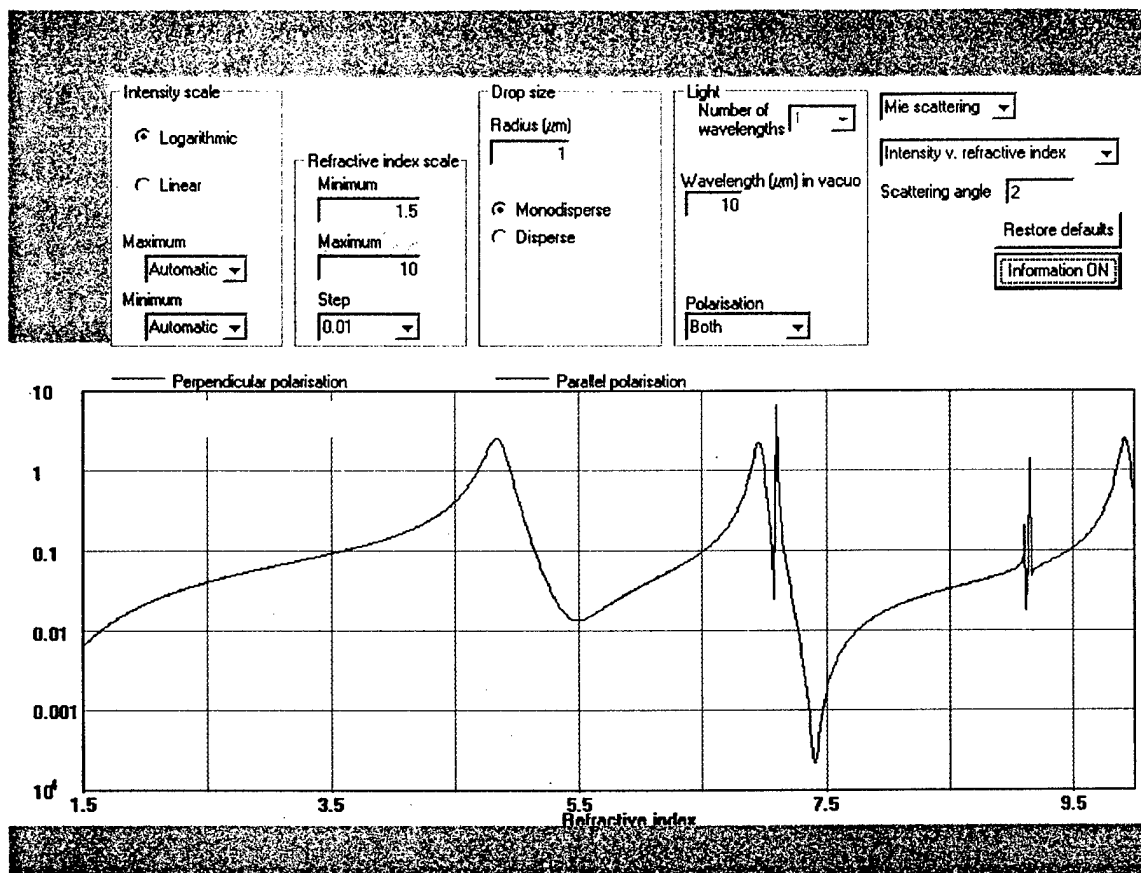
Figure 8.15 Intensity as a function of index of refraction for $\lambda/a = 10$ and $\theta = 2^0$
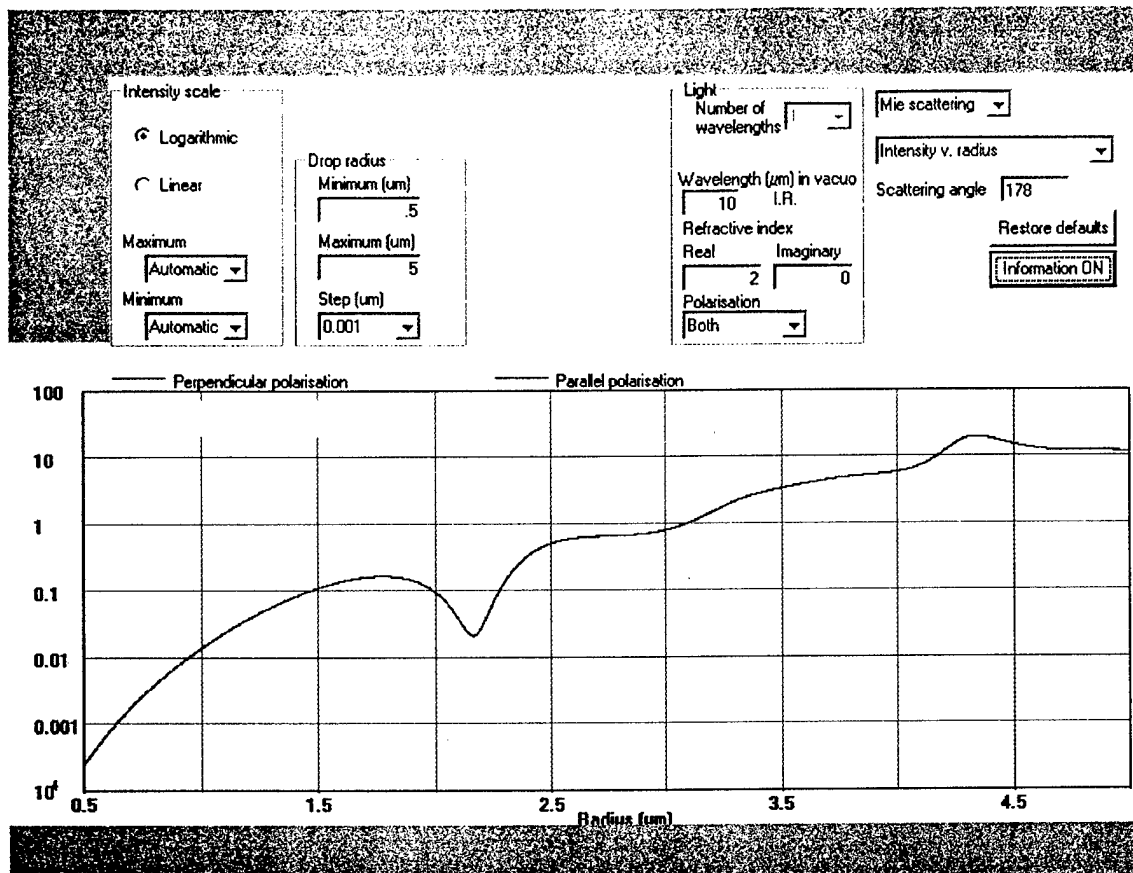
Figure 8.16 Intensity as a function of sphere radius for $\lambda = 10\mu m$ n= 2.0 and $\theta = 178^0$

Figs 8.16 – 8.21 show how the intensity of light scattered backwards, sideways and forward depends on the size of the sphere radius with $\lambda = 10\mu m$. The value of n is 2.0 in Figs 8.16 – 8.18, and n = 2.0 +20I in Figs 8.19 – 8.21. In all six Figures, the magnitude of the scattered intensity increases as the size of the spheres increases. Also note that the only significant polarization anisotropy occurs for sideway scattered light (Figs. 8.17 and 8.20).
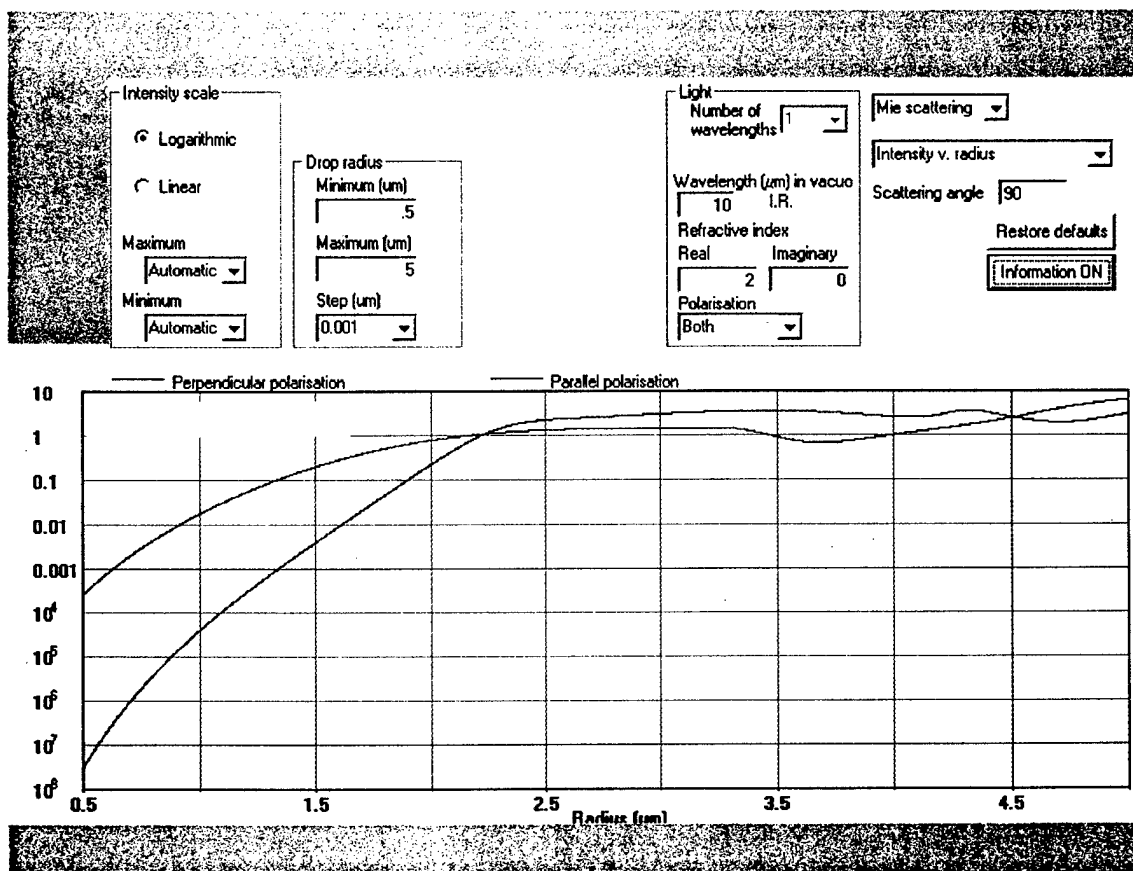
Figure 8.17 Intensity as a function of sphere radius for $\lambda = 10\mu m$ n= 2.0 and $\theta = 90^0$

Intensity scale

◉ Logarithmic

○ Linear

Maximum
Automatic ▾

Minimum
Automatic ▾

Drop radius
Minimum (um)
.5

Maximum (um)
5

Step (um)
0.001 ▾

Light
Number of wavelengths 1 ▾

Wavelength (μm) in vacuo
10   I.R.

Refractive index
Real   Imaginary
2   0

Polarisation
Both ▾

Mie scattering ▾

Intensity v. radius ▾

Scattering angle 2

Restore defaults

Information ON

——— Perpendicular polarisation   ——— Parallel polarisation

Radius (um)	Intensity

100
10
1
0.1
0.01
0.001
10⁴

0.5   1.5   2.5   3.5   4.5
Radius (um)

Figure 8.18 Intensity as a function of sphere radius for $\lambda = 10\mu m$ n= 2.0 and $\theta = 2^0$
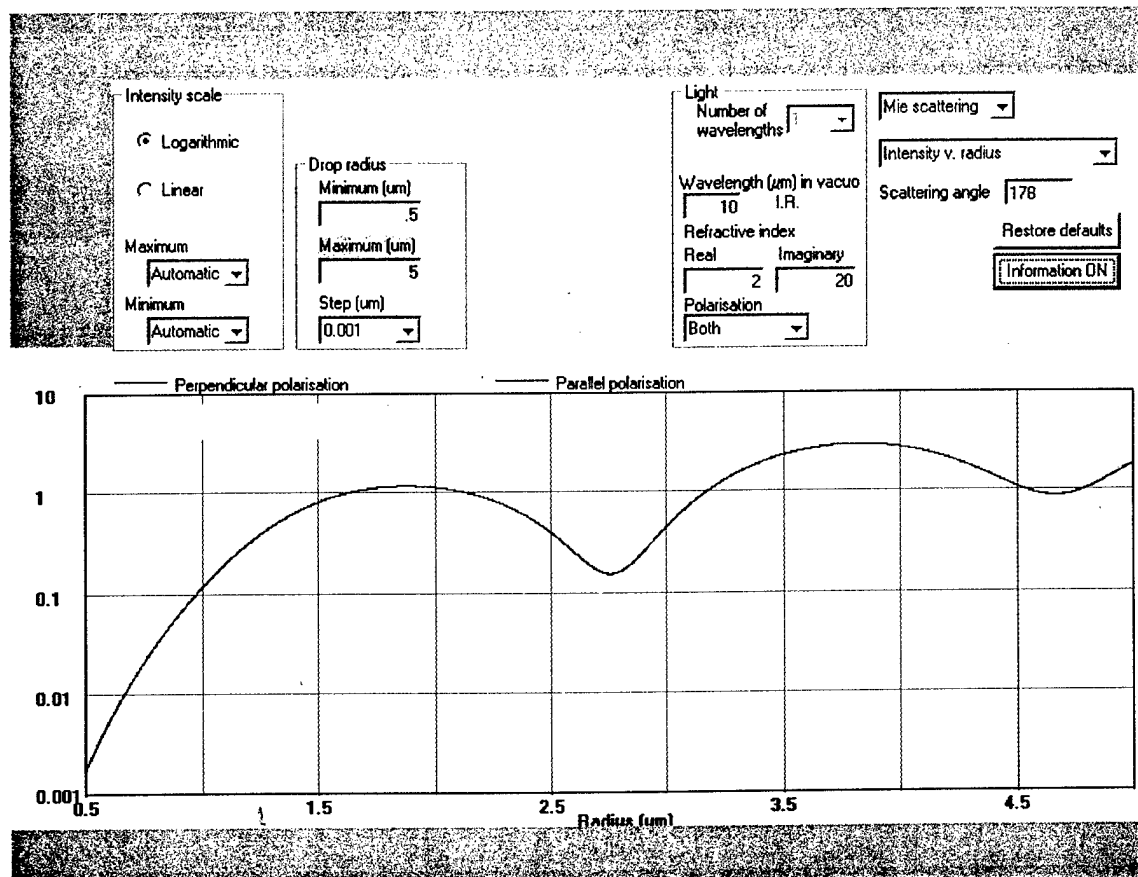
Figure 8.19 Intensity as a function of sphere radius for $\lambda = 10\mu m$ n= 2.0 + 20I and $\theta = 178^0$
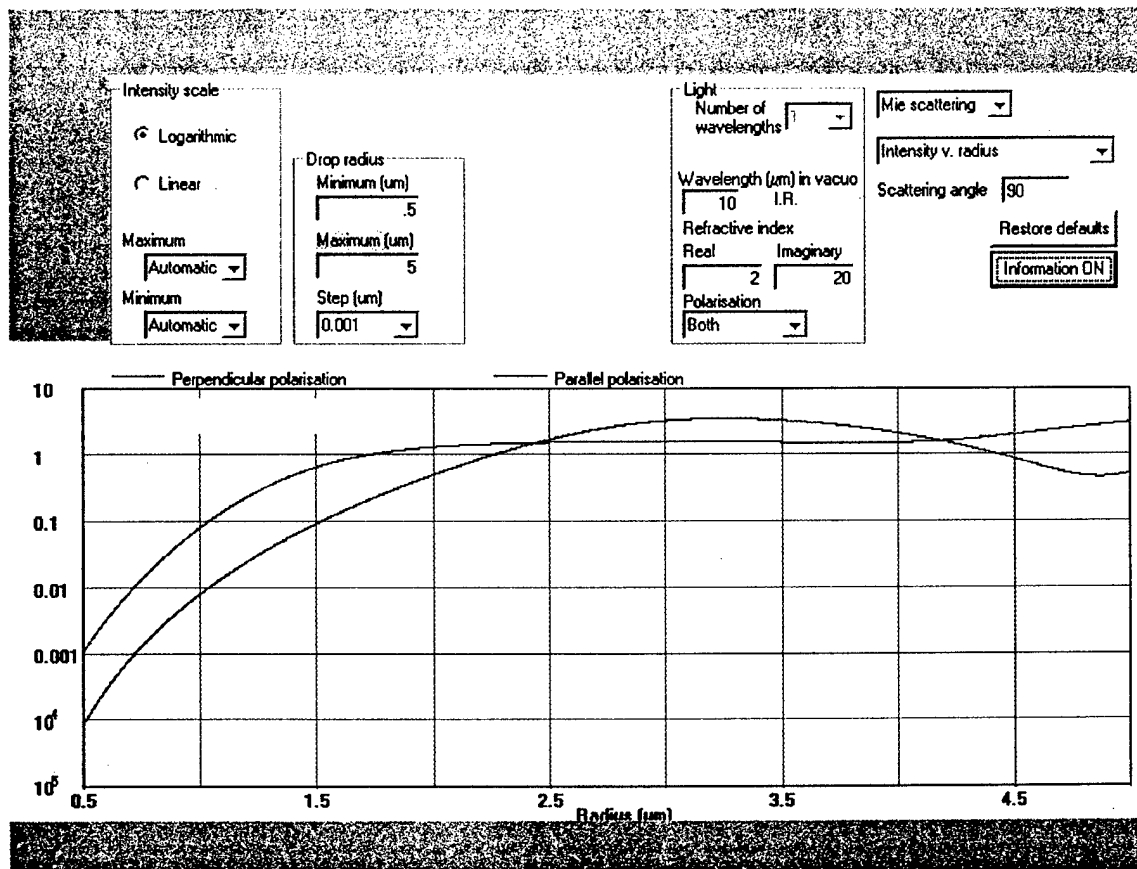
Figure 8.20 Intensity as a function of sphere radius for $\lambda = 10\mu m$ n= 2.0 + 20I and $\theta = 90^0$
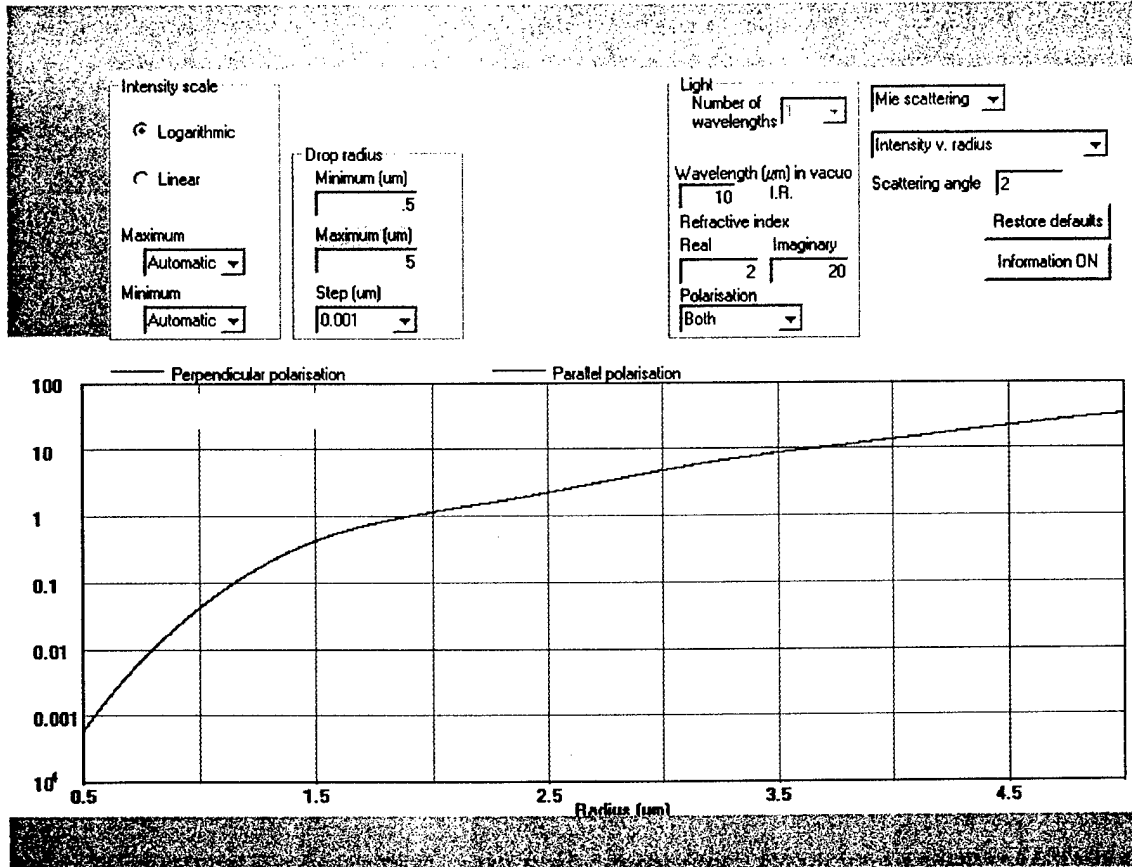
Figure 8.21 Intensity as a function of sphere radius for $\lambda = 10\mu m$ n= 2.0 + 20I and $\theta = 2^0$

8.4 Mie Scattering-Based Transport Model

Consider a polarized LWIR plane-wave propagates through a cylindrical column of air of radius ρ and length L. Assume that the only significant scattering in the column is due to aerosols that are smooth, uniform spheres. Let the number density of the "j" species of aerosols in the column be Aj, and the size distribution of species j be Pj[R]dR, where Pj[R] is the number of species j particles with a radius between R and R + dR. Then,

$$A_j = \int_{Rmin_j}^{Rmax_j} P_j [R] dR \qquad (8\text{-}19)$$

where,

$Rmax_j$ and $Rmin_j$ are the maximum and minimum radii of the jth species aerosols. As the geometric cross section of each sphere is πR^2, the column integrated aerosol geometric cross section G is approximately,

$$G \approx \pi\rho^2 L \sum_j \int_{Rmin_j}^{Rmax_j} \pi R^2 P_j[R]\,dR \qquad (8\text{-}20)$$

And, $\aleph$, the mean number of Mie scatterings per photon in the cylinder is the geometric cross section of all the aerosols divided by the cross sectional area of the cylinder

$$\aleph \sim G/\pi\rho^2 \qquad (8\text{-}21)$$

A quantitative transport model for multi-species Mie scattering can be developed in either a Monte Carlo or diffusion format.

9.0 REFERENCES

Adams, B., M. O. Smith and A. R. Gillespie, Simple models for complex material surfaces: A strategy for the hyperspectral era of remote sensing, *Proceeds of the IEEE International Geosciences Remote Sensing Symposium*, I, 16-21, 1989.

Arago, D.F., Extrait des Seances de l'Academie Rayale des Sciences (14 June), *Ann. Chem. Phys. Ser.*, 2(27):89, 1824.

Born, M. and Wolf, E. *Principles of Optics*, 1st Ed, Cambridge University Press, New York, NY, 1959.

Born, M. and Wolf, E. *Principles of Optics*, 7th Ed, Cambridge University Press, New York, NY, 2002.

Boardman, W., Automating spectral unmixing of AVIRIS data using convex geometry concepts, *Summaries of the Fourth Annual JPL Airborne Geosciences Workshop*, JPL Pub. 93-26, 11-14, 1993.

Coleman, R.F., *Light Scattering by Hexagonal Ice Crystals*, M.S. Thesis, Department of Meteorology, University of Utah, 1979.

Feofilov, P.P., *The Physical Basis of Polarized Emission*, Consultants Bureau, New York, 1961.

Gillespie, A. R., M. O. Smith, J. B. Adams, S. C. Willis, A. F. Fisher, and D. E. Sabol, Interpretation of residual images: Spectral mixture analysis of AVIRIS images, *Proceedings of*

the Second Airborne Visible/Infrared imaging Spectrometer (AVIRIS) Workshop, JPL Pub. 90-54, 1993.

Goody, R.M. and Yung, Y.L., *Atmospheric Radiation*, 2nd Ed., Oxford University Press, 1989.

Heiles, C. E., and Drake, F. S., The Polarization and Intensity of Thermal Radiation from a Planetary Surface, *Icarus*, 2, 281-292, 1963.

Hall Jr., F.F., The Polarized Emissivity of Water in the Infrared, *Applied Optics,* 3(6):781-782, 1964.

Hall, F.F., The Effects of Cirrus Clouds on 8 – 13μm Infrared Sky Radiance, *Applied Optics*, 7, 891, 1968.

Irvine, W.M. and Pollack, J.B., Infrared Optical Properties of Water and Ice Spheres, *Icarus* 8, 324, 1968.

Jackson, J. D., *Classical Electrodynamics*, John Wiley & Son, New York, 1962.

Jackson, J. D., *Classical Electrodynamics*, 3rd Ed., John Wiley & Sons, New York, 1999.

Jacobowitz, H., Emission, Scattering, and Absorption of Radiation in Cirrus Cloud Layers, Ph.D. Thesis, M.I.T, 1970.

Jacobowitz, H., A Method for Computing the Transfer of Solar Radiation Through Clouds of Hexagonal Ice Crystals, *J. Quant. Spect. Radiative Transfer* 11, 691, 1971.

Korb, A. R., P. Dybwad, W. Wadsworth, J. W. Salisbury, Portable Fourier Transform Infrared Spectroradiometer for Field Measurement of Radiance and Emissivity, *Applied Optics*, 35, No. 10, 1679-1692, 1996.

Lyot, B., Research on the Polarization of Light from Planets and from Some Terrestrial Substances, *Annals de L'Observatoire de Paris,* VIII (1), 1929.

Mie, G., *Ann. Physik*, 25, 377, 1908.

Millikan, R.A., A Study of the Polarization of the Light Emitted by Incandescent Solid and Liquid Surfaces, *Physics Review,* 3(81):177, 1895.

Ockmann, N., The Infrared and Raman Spectra of Ice, *Advan. Phys.* 7, 199, 1958.

Pesses, M. E., and Korb, A, Extension of subpixel demixing to polarimetric data, *Proceeding of the 1997 IRIS Specialty Group Meeting on Camouflage, Concealment and Deception*, October 1997.

Pesses, M. E., A. R. Korb, T. Coffey, and A. Stewart, Source Model And Target Detection Algorithms For Use With Intelligent IR Spectropolarimeters, Cont. # F29601-93-C-0211, VSSS/AFRL, May 1998.

Pesses, M. E., and A. Stewart, A hybrid approach to hyperspectral subpixel demixing, *Proceedings of the Third International Airborne Remote Sensing Conference*, Paper 11-5, 1997.

Schaaf, J.W. and Williams, D., Optical Constants of Ice in the Infrared, *JOSA*, 63, 726, 1973.

van de Hulst, H.C., *Light Scattering By Small Particles*, John Wiley, New York, 1957.

van de Hulst, H.C., Multiple *Light Scattering: Tables, Formulas, and Applications*, Two Volumes, Academic Press; 2, 1980.

Wendling, P., Wendling, R., and Weickmann, H. K., Scattering of Solar Radiation By Hexagonal Ice Crystals, *App. Optics.*, 18, 2663, 1979.

Appendix A: The Scattering Phase Function

Using Legendre polynomials we can expand the scattering phase function $\Phi(\cos\alpha)$ in a series of the form

$$\Phi(\cos\alpha) = \omega_0 \cdot P_0(\cos\alpha) + \omega_1 \cdot P_1(\cos\alpha) + \omega_2 P_2(\cos\alpha) + \ldots \ldots \quad (A.1)$$

where α is the angle of scattering, and $P_n(\cos\alpha)$ is the Legendre polynomial of order n. Conversely, we can obtain ω_n from

$$\omega_n = \left(\frac{2n+1}{2}\right) \int_{-1}^{+1} \Phi(\cos\alpha) P_n(\cos\alpha) d(\cos\alpha) \quad (A.2)$$

In particular, we know that

$$\omega_0 = 1 \quad , \quad P_0(\cos\alpha) = 1 \quad (A.3)$$

and

$$\omega_1 = 3g \quad , \quad P_1(\cos\alpha) = \cos\alpha \quad (A.4)$$

where g denotes the asymmetry factor. The normalized integral can be written

$$\frac{1}{2} \int_{-1}^{+1} \Phi(\cos\alpha) d(\cos\alpha) = 1 \quad (A.5)$$

and the asymmetry parameter can be obtained from

$$\frac{1}{2} \int_{-1}^{+1} \Phi(\cos\alpha) \cos\alpha \, d(\cos\alpha) = g \quad (A.6)$$

The fraction scattered in the forward hemisphere (f) is given by

$$\int_0^{+1} \Phi(\cos\alpha)\, d(\cos\alpha) = f \qquad (A.7)$$

Extreme values for the asymmetry parameter are:

g = 1 Complete Forward Scattering
g = 0 Isotropic Scattering
g = -1 Complete Background Scattering

Appendix-B: LWIR Hyper-Spectropolarimetric Measurement Methodology

B.1 Introduction

Spectropolarimetric information in the LWIR is more complex to reduce than unpolarized hyperspectral information. First, the amount of unique target information contained within the radiant flux of the LWIR is small and filtering the data will require longer dwell times. Second, to characterize the state of polarization, we need to filter the radiant flux to analyze the amount of polarization in that orientation. The second cause of increased complexity has downstream design issues; to quantify the linear polarization anisotropy either two systems need to acquire both polarizations with two different detectors simultaneously or a single detector array acquires the data serially with different orientations of the analyzing filters. Finally, each element of the optical path can attenuate the polarimetric sense of the target's radiant flux. Calibration of the raw data requires that these elements are accounted [Chipman, 1990].

In Appendix B we will highlight both our LWIR data acquisition and reduction techniques that support these tasks.

B.2 Methods

All of our data was collected at the US Army Topographic Engineering Center (TEC). The sensor was a Designs and Prototypes Fourier Transform Infrared Spectrometer. Approximately 250 spectral bands were collected in the 7 - 15 μm spectrum. Data were collected in analyzer positions $0°$, $45°$, $90°$ and $135°$ to derive Stokes parameters S_0, S_1, and S_2 (Korb, et al. 1996).
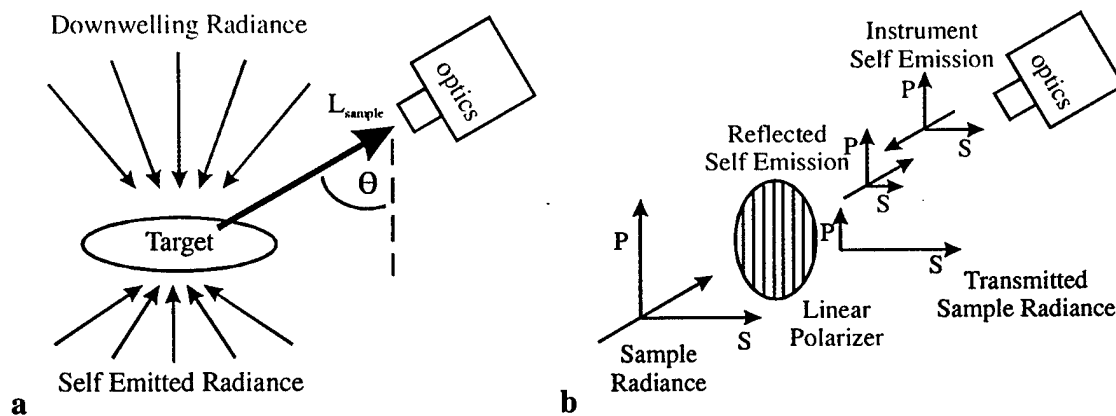
Figure B-1 Elements of the Optical Path (a) Environmental Effects
(b) Polarization Analyzer Effects

B.3 Calibration

For radiometry, raw data voltages are calibrated using known blackbody temperatures. Often, the data is interpolated linearly between the blackbody sources that bracket the range of expected target and downwelling radiance temperatures. With spectro-polarimetry, an additional source is put into the optical path, the linear polarizing filters (Figure **B-1**). Although the blackbody radiators are expected to be unpolarized, the energy transmitted by the polarizers passes though the FTIR's optics that may be sensitive to polarization. This polarization sensitivity may be a function of optical telescopes angle with respect to nadir.

Notes for Equations:	Subscripts
V_x = raw voltage	H = high blackbody temperature
T_x = temperature	A = low blackbody temperature
B_x = computed Planck function at temperature T	DWR = downwelling radiance plate
	G = gold plate
ε = emissivity	inst = instrument
r = responsivity	λ = wavelength

Table B-1 Terms and Subscripts

In order to compensate for possible polarimetric effects in the optical path, the following procedures have been added to the calibration process. The FTIR images the blackbodies in the same orientation of the telescope relative the surface normal as the sample and downwelling radiance calibration wedge. The FTIR images the blackbody in the same filter orientation as the sample and the calibration plate (Figure B-2). The calibration is performed by linear interpolation of the observed blackbody temperatures to the computed Planck functions at the same temperatures. In addition to the sample temperatures, the calibration plate radiances were also calibrated against known blackbody temperatures.

$$r(\lambda) = \frac{V_H(\lambda) - V_A(\lambda)}{B(T_H, \lambda) - B(T_A, \lambda)} \qquad L^o(T_{inst}, \lambda) = B(T_A, \lambda) - \frac{V_A(\lambda)}{r(\lambda)}$$

$$L_s(\lambda) = \frac{V_S(\lambda)}{r(\lambda)} + L^o(\lambda, T_{inst})$$

Figure B-2 Mathematical progression for converting raw radiance to calibrated radiance

B.4 Plate Correction

Each of the calibrated downwelling samples was corrected for plate temperature. The downwelling radiance was recorded by observing a sample of known emissivity. As with the conversion of raw to calibrated data, the conversion of calibrated downwelling radiances to corrected downwelling radiance was performed for each of the orientations of the polarization filters. The SAIC team used rough gold and aluminum plates to estimate downwelling radiance at a known emissivity. The temperature of these downwelling radiance calibration plates was recorded at the time they were observed. Knowing both the temperature and emissivity of an object enables the separation of reflected and emitted spectra of the known sample and apply that ratio to unknown samples.

$$L_{DWR,meas}(\lambda) = L_{DWR}(\lambda)(1 - \varepsilon_G(\lambda)) + \varepsilon_G(\lambda)B(T_G, \lambda)$$

$$L_{DWR}(\lambda) = \frac{L_{DWR,meas}(\lambda) - \varepsilon_G(\lambda)B(T_G, \lambda)}{(1 - \varepsilon_G(\lambda))}$$

Figure B-3 Conversion of raw radiance from the calibration plate to calibrated radiance

B.5 Reflectance/Emission Separation

The absolute emissivity of the target was derived by using the known relationship between observed and ideal response of a known object and applying that relationship to unknown targets. The corrected downwelling radiance file provides the relationship between observed and ideal conditions. The corrected downwelling radiance files are applied to the calibrated target files to generate absolute emissivity. The corrected downwelling radiance files are only suitable for their specific filter orientation.

$$\varepsilon_S(\lambda) = \frac{L_S(\lambda) - L_{DWR}(\lambda)}{B(\lambda, T_S) - L_{DWR}(\lambda)}$$

Figure B.4 Separation of reflectance and emittance

B.6 Stokes Parameters

After reducing the data, computing the Stokes parameters is trivial. Let $0°$ and $90°$ to be a surrogate orientation of the analyzing polarizing filters in the in-plane and out of plane of polarization, i.e., the 'H' and 'V' polarizations. The computation of the Stokes parameters is produced for each wavelength (Figure B-5). From this, the linear polarization anisotropy is the quotient of S_1 and S_2.

$$S_o(\lambda) = \varepsilon_V + \varepsilon_H$$
$$S_1(\lambda) = \varepsilon_V - \varepsilon_H$$
$$S_2(\lambda) = \varepsilon_{V+45°} - \varepsilon_{H+45°}$$

Figure B-5 Computation of the Stokes parameters

Appendix C: SAIC LWIR Spectropolarimetric Modeling

C.1 Introduction
The extension of microfacet based scattering models from intensity to polarimetric has been reported by AFRL-Kirtland In support of the Eyeball program SAIC has also developed a spectropolarimetric microfacet model for predicting target and background signatures in the 8-14 μm region. The SAIC model's computational approach is based on the Born-Wolf coherence matrix and seamlessly integrates self-emitted and reflected radiation. Thermal self-emission is assumed to be transmitted internal blackbody radiation that is modified by passing through the change in the index of refraction that occurs at the surface-air interface. Both the self-emission and reflection model uses textbook Fresnel formulas and are in very good agreement with laboratory observations.

The evaluation of the Fresnel reflection coefficients requires knowledge of the index of refraction (n) and magnetic permeability of the reflecting surface and air. Also required are the value of the angle ϕ between the microfacet surface normal unit vector (**n**) and the Poynting vector **k** of the reflected wave and the value of the angle ψ between **n** and the Poynting vector of the transmitted wave. If the index or refraction is real this is not a problem, but if n is complex the value of ψ is also complex. In this situation we used the Born and Wolf derived effective value for ψ that has the property of conservation of energy in the transmission processes.

C.2 Coordinate Systems
Microfacet pixel models like ours are based on the assumption that the radiation emanating from each microfacet in the pixel can be combined incoherently at the detector. In order for this assumption to be true, the pixel surface roughness correlation length must be much, much larger than the coherence length of the reflected and emitted radiation. When this condition is met, intensities for different ray paths can be added as their mutual coherence term is zero, and there is negligible diffraction of light off microfacet edges. Under these conditions, each microfacet can be approximated by a smooth flat surface and the radiation emanating from each microfacet can be modeled using the Fresnel equations.

The directions of the Ep and Es components of the electric field **E** are shown in Figure C.1. Here, **k** is the Poynting vector of the radiation observed at the sensor and **n** is the microfacet surface normal vector direction. It is important to note that the Fresnel equations are only valid in the coordinate system shown in Figs. C.1 and C.2, and that this is a locally defined system and that the directions of Ep and Es vary with sensor location. On the other hand, the location of each scene object, each sensor, the center of each scene pixel, and the center of each sky patch are defined in a global coordinate system. The direction of the mean surface normal vector **m** of each pixel is also defined in the global coordinate system, while the direction of **n** is defined locally relative to **m** and also defined globally.
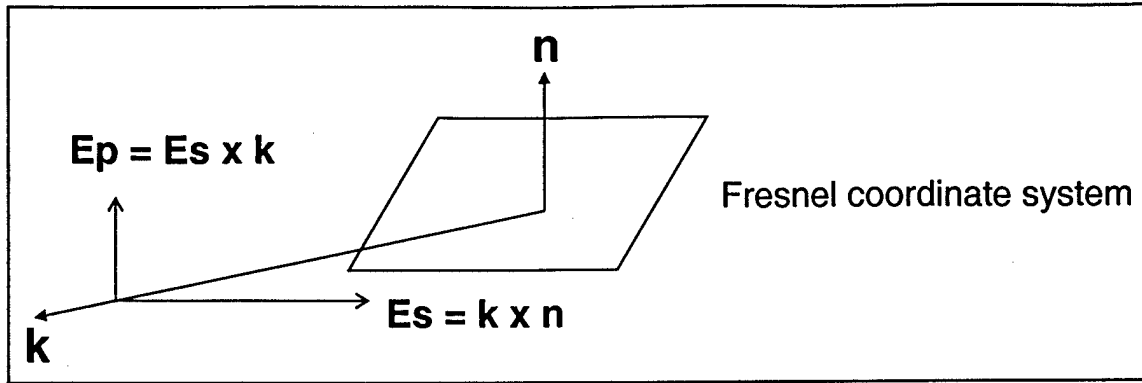
Figure C-1. The Fresnel coordinate system.
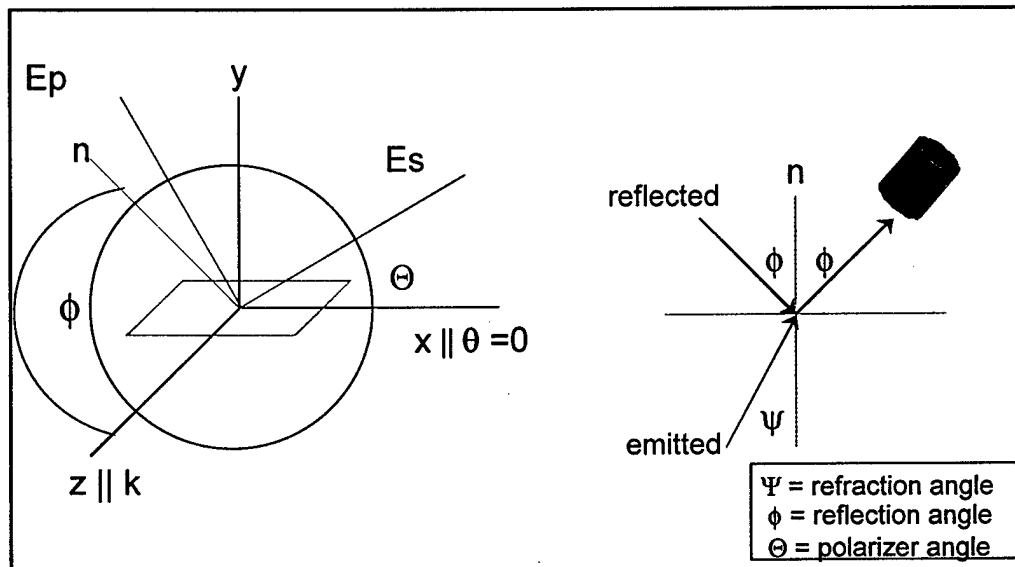
Figure C-2. Definition of angles

The evaluation of the angle ϕ between $\mathbf{n}$ and the sensor position $\mathbf{R}$ and the evaluation of the angle ρ between $\mathbf{n}$ and sky patch $\mathbf{r}$ are carried out in the global coordinate system. Figure 2 depicts the angles ϕ and ψ, as well as the angle Θ between the Es component of $\mathbf{E}$ and the linear polarization filter angle $\theta = 0°$ setting.

C.3 Intensity Equations

In the evaluation of these equations we assume that distance between a pixel and a sensor, is much, much greater than the size of a pixel. Therefore, no accuracy is lost by assuming that all microfacets are located at the center of a pixel. If both the temperature and index of refraction are constant and uniform over a microfacet surface (but not necessarily the same from one microfacet to the next), the observed intensity emanating from a microfacet as a function of

viewing geometry and polarizer filter settings is given by Eq. (C-1), where the Born Wolf parameters are for sake of computational ease presented as a 4-vector $\vec{J}$.

$$I_S\left(\theta,\alpha,\lambda,\phi_S,\Theta_S\right) =$$

$$\{[\vec{J}_T\left(\lambda,\psi_S\right)\bullet\ddot{F}_T\left(\lambda,\psi_S,\phi_S\right)+\vec{J}_R\left(\lambda,\phi_S\right)\bullet\ddot{F}_R\left(\lambda,\phi_S,\psi_S\right)]\bullet\ddot{M}\left(\Theta_S\right)\}\bullet\vec{T}\left(\theta,\alpha\right) \qquad \text{(C.1)}$$

In (C.1)

$$\vec{J}_T = \begin{pmatrix} J_{SS}^T \\ J_{PP}^T \\ J_{SP}^T \\ J_{PS}^T \end{pmatrix} \qquad \vec{J}_R = \begin{pmatrix} J_{SS}^R \\ J_{PP}^R \\ J_{SP}^R \\ J_{PS}^R \end{pmatrix} \qquad \text{(C.2)}$$

where, the subscripts and superscripts "T" and "R" referrer to the coherence vector of the internal transmitted and external reflected radiation sources.

$$\ddot{F}_T = \begin{bmatrix} F_S^T F_S^{T*} & 0 & 0 & 0 \\ 0 & F_P^T F_P^{T*} & 0 & 0 \\ 0 & 0 & F_S^T F_P^{T*} & 0 \\ 0 & 0 & 0 & F_P^T F_S^{T*} \end{bmatrix} Coe \qquad \text{(C.3)}$$

$$\ddot{F}_R = \begin{bmatrix} F_S^R F_S^{R*} & 0 & 0 & 0 \\ 0 & F_P^R F_P^{R*} & 0 & 0 \\ 0 & 0 & F_S^R F_P^{R*} & 0 \\ 0 & 0 & 0 & F_P^R F_S^{R*} \end{bmatrix} \qquad \text{(C.4)}$$

here, Fs and Fp are the Fresnel coefficients for the s and p components of E and the superscripts "T" and "R" referrer the Fresnel coefficients for transmission and reflection. The superscript "*" means complex conjugant. Coe is the conservation of energy term for transmitted light, where n_a and n_s are the index of refraction of the air and surface respectively.

$$Coe = \frac{n_a \cos(\phi)}{n_s \cos(\psi)} \qquad \text{(C.5)}$$

and,

$$\tilde{F}_T\left(\lambda,\psi,\phi\right)+\tilde{F}_R\left(\lambda,\phi,\psi\right)=\tilde{I} \tag{C.6}$$

Also in (C.1)

$$\tilde{M}=\begin{bmatrix} C^2 & S^2 & CS & CS \\ S^2 & C^2 & -CS & -CS \\ -CS & CS & C^2 & -S^2 \\ -CS & CS & -S^2 & C^2 \end{bmatrix} \tag{C.7}$$
$$C=\mathrm{Cos}\left(\Theta\right)\ S=\mathrm{Sin}\left(\Theta\right)$$

$$\tilde{T}=\begin{pmatrix} \mathrm{Cos}^2\left(\theta\right) \\ \mathrm{Sin}^2\left(\theta\right) \\ e^{-i\alpha}\mathrm{Cos}\left(\theta\right)\mathrm{Sin}\left(\theta\right) \\ e^{+i\alpha}\mathrm{Cos}\left(\theta\right)\mathrm{Sin}\left(\theta\right) \end{pmatrix} \tag{C.8}$$

Above, θ is the linear polarization filter angle and α is the quarter-waveplate retardance angel.

A-9

Appendix D: Exact Solution to Mie Scattering Problem.

The Mathematic™ v4.2 code used in the study is presented below.

```
"Exact Uniform Sphere Mie Scattering ";
"l is sumation indix";
BJ[r_, l_] := Sqrt[Pi * r / 2] * BesselJ [l, r + 1 / 2]
BY[r_, l_] := Sqrt[Pi * r / 2] * BesselY [l, r + 1 / 2]
BH[r_, l_] := BJ[r, l] - I * BY[r, l]
```

$$
DBJ[r\_, l\_] := Sqrt[Pi / 2] * \left(r\, BesselJ\left[-1 + l, \frac{1}{2} + r\right] \right.
$$

$$
+ BesselJ\left[l, \frac{1}{2} + r\right]
$$

$$
\left. - r\, BesselJ\left[1 + l, \frac{1}{2} + r\right] \right) \Big/ 2 \Big/ Sqrt[r]
$$

$$
DBH[r\_, l\_] := \frac{1}{2\sqrt{r}} \left(\sqrt{\frac{\pi}{2}} \left(r\, BesselJ\left[-1 + l, \frac{1}{2} + r\right] \right. \right.
$$

$$
+ BesselJ\left[l, \frac{1}{2} + r\right]
$$

$$
- r\, BesselJ\left[1 + l, \frac{1}{2} + r\right] - i \left(r\, BesselY\left[-1 + l, \frac{1}{2} + r\right] \right.
$$

$$
+ BesselY\left[l, \frac{1}{2} + r\right]
$$

$$
\left. \left. \left. - r\, BesselY\left[1 + l, \frac{1}{2} + r\right] \right) \right) \right)
$$

```
"n is the complex index of refraction of sphere ";
"n = 1 for region outside of sphere ";
n=.
"μ=Cos[θ] ";
"q = 2πa/λ";
"a = radius of sphere ";
"λ = wavelength of light ";
eB[n_, q_, l_] := (I) ^ (l + 1) * (2 * l + 1) *
   (n * DBJ[q, l] * BJ[n * q, l] - BJ[q, l] * DBJ[n * q, l] ) /
      (l * (l + 1)) /
   (n * DBH[q, l] * BJ[n * q, l] - BH[q, l] * DBJ[n * q, l])
mB[n_, q_, l_] := (I) ^ (l + 1) * (2 * l + 1) *
   (n * BJ[q, l] * DBJ[n * q, l] - DBJ[q, l] * BJ[n * q, l] ) /
      (l * (l + 1)) /
   (n * BH[q, l] * DBJ[n * q, l] - DBH[q, l] * BJ[n * q, l])
LP1[μ_, l_] := LegendreP [l, 1, μ]
LP[μ_, l_] := LegendreP [l, μ]
DrLP1[μ_, l_] := D[LP1 [μ, l], μ]
"Es and Ep are the components of the electric
   field vector in the local Fresnel coordinate system ";
```

```
Es[μ_, l_, n_, a_, λ_] :=
  (λ / 2 Pi) * (-I)^l * (eB[n, 2 Pi * a / λ, l] * DrLP1[μ, l] * Sqrt[1 - μ^2] -
    mB[n, 2 Pi * a / λ, l] * LP1[μ, l] / Sqrt[1 - μ^2])
Ep[μ_, l_, n_, a_, λ_] :=
  (λ / 2 Pi) * (-I)^l * (eB[n, 2 Pi * a / λ, l] * LP1[μ, l] / Sqrt[1 - μ^2] -
    mB[n, 2 Pi * a / λ, l] * DrLP1[μ, l] * Sqrt[1 - μ^2])
"Is and Ip are the intenisities  of components  of the
    electric  field  vector  in the  local  Fresnel  coordinate  system";
μ =.
Is[μ_, n_, a_, λ_, S_] :=
 Abs[Sum[Es[μ, l, n, a, λ], {l, 1, S}]]^2
Ip[μ_, n_, a_, λ_, S_] :=
  Abs[Sum[Ep[μ, l, n, a, λ], {l, 1, S}]]^2;
```

Table 1. Arctic Winter Atmospheric Model

Altitude (km)	Pressure (Mb)	T (deg K)	T (deg C)	Number Density (m^{-3})	
				Total	Water Vapor
0.0	1.018E+03	249.20	-23.95	2.959E+25	2.007E+22
1.0	8.879E+02	251.20	-21.95	2.560E+25	2.141E+22
2.0	7.749E+02	249.70	-23.45	2.248E+25	1.773E+22
3.0	6.752E+02	246.00	-27.15	1.988E+25	1.238E+22
4.0	5.867E+02	240.70	-32.45	1.765E+25	7.360E+21
5.0	5.082E+02	235.60	-37.55	1.562E+25	4.349E+21
6.0	4.386E+02	228.20	-44.95	1.392E+25	2.342E+21
7.0	3.767E+02	222.10	-51.05	1.228E+25	1.004E+21
8.0	3.225E+02	217.70	-55.45	1.073E+25	3.346E+20
9.0	2.752E+02	213.80	-59.35	9.323E+24	2.810E+20
10.0	2.343E+02	211.20	-61.95	8.035E+24	1.840E+20
11.0	1.991E+02	209.50	-63.65	6.884E+24	1.271E+20
12.0	1.692E+02	210.50	-62.65	5.822E+24	8.699E+19
13.0	1.439E+02	210.70	-62.45	4.947E+24	6.022E+19
14.0	1.223E+02	209.20	-63.95	4.234E+24	3.346E+19
15.0	1.052E+02	207.95	-65.20	3.664E+24	2.743E+19
16.0	8.810E+01	206.70	-66.45	3.087E+24	2.141E+19
17.0	7.570E+01	205.95	-67.20	2.662E+24	1.907E+19
18.0	6.320E+01	205.20	-67.95	2.231E+24	1.673E+19
19.0	5.425E+01	204.95	-68.20	1.917E+24	1.589E+19
20.0	4.530E+01	204.70	-68.45	1.603E+24	1.506E+19
21.0	3.830E+01	205.20	-67.95	1.352E+24	1.706E+19
22.0	3.240E+01	205.20	-67.95	1.144E+24	1.706E+19
23.0	2.750E+01	208.20	-64.95	9.567E+23	1.807E+19
24.0	2.330E+01	211.90	-61.25	7.964E+23	2.007E+19
25.0	1.970E+01	211.30	-61.85	6.753E+23	2.242E+19
30.0	1.020E+01	216.00	-57.15	3.420E+23	1.204E+19
35.0	4.701E+00	222.30	-50.85	1.532E+23	3.680E+18
40.0	2.243E+00	234.70	-38.45	6.922E+22	1.439E+18
45.0	1.113E+00	247.00	-26.15	3.264E+22	6.357E+17
50.0	5.719E-01	259.30	-13.85	1.598E+22	2.108E+17
70.0	5.200E-02	245.70	-27.45	1.533E+21	4.684E+15
100.0	3.200E-04	210.00	-63.15	1.104E+19	3.346E+13

Table 2. Sub Arctic Winter Atmospheric Model

Altitude (km)	Pressure (Mb)	T (deg K)	T (deg C)	Number Density (m^{-3})	
				Total	Water Vapor
0.0	1.013E+03	257.20	-15.95	2.853E+25	4.015E+22
1.0	8.878E+02	259.10	-14.05	2.482E+25	4.015E+22
2.0	7.775E+02	255.90	-17.25	2.201E+25	3.145E+22
3.0	6.798E+02	252.70	-20.45	1.949E+25	2.275E+22
4.0	5.932E+02	247.70	-25.45	1.735E+25	1.372E+22
5.0	5.158E+02	240.90	-32.25	1.551E+25	6.691E+21
6.0	4.467E+02	234.10	-39.05	1.382E+25	3.279E+21
7.0	3.853E+02	227.30	-45.85	1.228E+25	1.807E+21
8.0	3.308E+02	220.60	-52.55	1.086E+25	3.680E+20
9.0	2.829E+02	217.20	-55.95	9.434E+24	2.810E+20
10.0	2.418E+02	217.20	-55.95	8.063E+24	1.840E+20
11.0	2.067E+02	217.20	-55.95	6.893E+24	1.271E+20
12.0	1.766E+02	217.20	-55.95	5.889E+24	8.699E+19
13.0	1.510E+02	217.20	-55.95	5.036E+24	6.022E+19
14.0	1.291E+02	217.20	-55.95	4.305E+24	3.346E+19
15.0	1.103E+02	217.20	-55.95	3.678E+24	2.543E+19
16.0	9.430E+01	216.60	-56.55	3.153E+24	2.141E+19
17.0	8.060E+01	216.00	-57.15	2.703E+24	1.874E+19
18.0	6.880E+01	215.40	-57.75	2.313E+24	1.673E+19
19.0	5.880E+01	214.80	-58.35	1.983E+24	1.639E+19
20.0	5.010E+01	214.20	-58.95	1.694E+24	1.506E+19
21.0	4.280E+01	213.60	-59.55	1.451E+24	1.706E+19
22.0	3.650E+01	213.00	-60.15	1.241E+24	1.706E+19
23.0	3.110E+01	212.40	-60.75	1.061E+24	1.807E+19
24.0	2.650E+01	211.80	-61.35	9.062E+23	2.007E+19
25.0	2.260E+01	211.20	-61.95	7.751E+23	2.242E+19
30.0	1.020E+01	216.00	-57.15	3.420E+23	1.204E+19
35.0	4.700E+00	222.30	-50.85	1.531E+23	3.680E+18
40.0	2.200E+00	234.70	-38.45	6.789E+22	1.439E+18
45.0	1.100E+00	247.00	-26.15	3.226E+22	6.357E+17
50.0	6.000E-01	259.30	-13.85	1.676E+22	2.108E+17
70.0	5.200E-02	245.70	-27.45	1.533E+21	4.684E+15
100.0	3.200E-04	210.00	-63.15	1.104E+19	3.346E+13

Table 3. Mid Latitude Winter Atmospheric Model

Altitude (km)	Pressure (Mb)	T (deg K)	T (deg C)	Number Density (m^{-3})	
				Total	Water Vapor
0.0	1.018E+03	272.20	-0.95	2.709E+25	1.171E+23
1.0	8.973E+02	268.70	-4.45	2.419E+25	8.364E+22
2.0	7.897E+02	265.20	-7.95	2.157E+25	6.022E+22
3.0	6.938E+02	261.70	-11.45	1.920E+25	4.015E+22
4.0	6.081E+02	255.70	-17.45	1.723E+25	2.208E+22
5.0	5.313E+02	249.70	-23.45	1.541E+25	1.271E+22
6.0	4.627E+02	243.70	-29.45	1.375E+25	7.026E+21
7.0	4.016E+02	237.70	-35.45	1.224E+25	2.844E+21
8.0	3.473E+02	231.70	-41.45	1.086E+25	1.171E+21
9.0	2.993E+02	225.70	-47.45	9.605E+24	5.353E+20
10.0	2.568E+02	219.70	-53.45	8.466E+24	2.509E+20
11.0	2.199E+02	219.20	-53.95	7.266E+24	2.308E+20
12.0	1.882E+02	218.70	-54.45	6.233E+24	2.007E+20
13.0	1.611E+02	218.20	-54.95	5.348E+24	6.022E+19
14.0	1.378E+02	217.70	-55.45	4.585E+24	3.346E+19
15.0	1.178E+02	217.20	-55.95	3.928E+24	2.543E+19
16.0	1.007E+02	216.70	-56.45	3.366E+24	2.141E+19
17.0	8.610E+01	216.20	-56.95	2.885E+24	1.874E+19
18.0	7.360E+01	215.70	-57.45	2.471E+24	1.673E+19
19.0	6.280E+01	215.20	-57.95	2.114E+24	1.639E+19
20.0	5.370E+01	215.20	-57.95	1.807E+24	1.506E+19
21.0	4.580E+01	215.20	-57.95	1.542E+24	1.706E+19
22.0	3.910E+01	215.20	-57.95	1.316E+24	1.706E+19
23.0	3.340E+01	215.20	-57.95	1.124E+24	1.807E+19
24.0	2.860E+01	215.20	-57.95	9.626E+23	2.007E+19
25.0	2.440E+01	215.20	-57.95	8.212E+23	2.242E+19
30.0	1.110E+01	217.40	-55.75	3.698E+23	1.204E+19
35.0	5.200E+00	227.90	-45.25	1.653E+23	3.680E+18
40.0	2.500E+00	243.20	-29.95	7.446E+22	1.439E+18
45.0	1.300E+00	258.50	-14.65	3.643E+22	6.357E+17
50.0	7.000E-01	265.70	-7.45	1.908E+22	2.108E+17
70.0	5.200E-02	230.70	-42.45	1.633E+21	4.684E+15
100.0	3.200E-04	210.20	-62.95	1.103E+19	3.346E+13

Table 4. Sub Arctic Summer Atmospheric Model

Altitude (km)	Pressure (Mb)	T (deg K)	T (deg C)	Number Density (m^{-3})	
				Total	Water Vapor
0.0	1.010E+03	287.20	14.05	2.547E+25	3.045E+23
1.0	8.960E+02	281.70	8.55	2.304E+25	2.007E+23
2.0	7.929E+02	276.30	3.15	2.079E+25	1.405E+23
3.0	7.000E+02	270.90	-2.25	1.872E+25	9.033E+22
4.0	6.160E+02	265.50	-7.65	1.681E+25	5.688E+22
5.0	5.410E+02	260.10	-13.05	1.507E+25	3.346E+22
6.0	4.740E+02	253.10	-20.05	1.356E+25	1.807E+22
7.0	4.130E+02	246.10	-27.05	1.216E+25	9.702E+21
8.0	3.590E+02	239.20	-33.95	1.087E+25	4.349E+21
9.0	3.108E+02	232.20	-40.95	9.695E+24	1.405E+21
10.0	2.677E+02	225.20	-47.95	8.610E+24	5.018E+20
11.0	2.300E+02	225.20	-47.95	7.398E+24	3.145E+20
12.0	1.977E+02	225.20	-47.95	6.359E+24	2.007E+20
13.0	1.700E+02	225.20	-47.95	5.468E+24	6.022E+19
14.0	1.460E+02	225.20	-47.95	4.696E+24	3.346E+19
15.0	1.260E+02	225.20	-47.95	4.053E+24	2.543E+19
16.0	1.080E+02	225.20	-47.95	3.474E+24	2.141E+19
17.0	9.280E+01	225.20	-47.95	2.985E+24	1.874E+19
18.0	7.980E+01	225.20	-47.95	2.567E+24	1.673E+19
19.0	6.860E+01	225.20	-47.95	2.206E+24	1.639E+19
20.0	5.900E+01	225.20	-47.95	1.898E+24	1.506E+19
21.0	5.070E+01	225.20	-47.95	1.631E+24	1.706E+19
22.0	4.360E+01	225.20	-47.95	1.402E+24	1.706E+19
23.0	3.750E+01	225.20	-47.95	1.206E+24	1.807E+19
24.0	3.230E+01	226.60	-46.55	1.032E+24	2.007E+19
25.0	2.780E+01	228.10	-45.05	8.828E+23	2.242E+19
30.0	1.340E+01	235.10	-38.05	4.128E+23	1.204E+19
35.0	6.600E+00	247.20	-25.95	1.934E+23	3.680E+18
40.0	3.400E+00	262.10	-11.05	9.396E+22	1.439E+18
45.0	1.800E+00	277.65	4.50	4.696E+22	6.357E+17
50.0	1.000E+00	277.20	4.05	2.613E+22	2.108E+17
70.0	5.200E-02	216.60	-56.55	1.739E+21	4.684E+15
100.0	3.200E-04	210.00	-63.15	1.104E+19	3.346E+13

Table 5. Mid latitude Summer Atmospheric Model

Altitude (km)	Pressure (Mb)	T (deg K)	T (deg C)	Number Density (m^{-3})	
				Total	Water Vapor
0.0	1.013E+03	294.20	21.05	2.494E+25	4.684E+23
1.0	9.020E+02	289.70	16.55	2.255E+25	3.111E+23
2.0	8.020E+02	285.20	12.05	2.037E+25	1.974E+23
3.0	7.100E+02	279.20	6.05	1.842E+25	1.104E+23
4.0	6.280E+02	273.20	0.05	1.665E+25	6.357E+22
5.0	5.540E+02	267.20	-5.95	1.502E+25	3.346E+22
6.0	4.870E+02	261.20	-11.95	1.350E+25	2.041E+22
7.0	4.260E+02	254.70	-18.45	1.211E+25	1.238E+22
8.0	3.720E+02	248.20	-24.95	1.086E+25	7.026E+21
9.0	3.240E+02	241.70	-31.45	9.709E+24	4.015E+21
10.0	2.810E+02	235.30	-37.85	8.650E+24	2.141E+21
11.0	2.430E+02	228.80	-44.35	7.693E+24	7.360E+20
12.0	2.090E+02	222.30	-50.85	6.810E+24	2.007E+20
13.0	1.790E+02	215.80	-57.35	6.008E+24	6.022E+19
14.0	1.530E+02	215.70	-57.45	5.138E+24	3.346E+19
15.0	1.300E+02	215.70	-57.45	4.365E+24	2.543E+19
16.0	1.110E+02	215.70	-57.45	3.727E+24	2.141E+19
17.0	9.500E+01	215.70	-57.45	3.190E+24	1.874E+19
18.0	8.120E+01	216.80	-56.35	2.713E+24	1.673E+19
19.0	6.950E+01	217.90	-55.25	2.310E+24	1.639E+19
20.0	5.950E+01	219.20	-53.95	1.966E+24	1.506E+19
21.0	5.100E+01	220.40	-52.75	1.676E+24	1.706E+19
22.0	4.370E+01	221.60	-51.55	1.428E+24	1.706E+19
23.0	3.760E+01	222.80	-50.35	1.222E+24	1.807E+19
24.0	3.220E+01	223.90	-49.25	1.042E+24	2.007E+19
25.0	2.770E+01	225.10	-48.05	8.913E+23	2.242E+19
30.0	1.320E+01	233.70	-39.45	4.091E+23	1.204E+19
35.0	6.500E+00	245.20	-27.95	1.920E+23	3.680E+18
40.0	3.300E+00	257.50	-15.65	9.282E+22	1.439E+18
45.0	1.800E+00	269.90	-3.25	4.831E+22	6.357E+17
50.0	1.000E+00	275.70	2.55	2.627E+22	2.108E+17
70.0	5.200E-02	218.10	-55.05	1.727E+21	4.684E+15
100.0	3.200E-04	210.00	-63.15	1.104E+19	3.346E+13

Table 6. Tropic Atmospheric Model

Altitude (km)	Pressure (Mb)	T (deg K)	T (deg C)	Number Density (m⁻³)	
				Total	Water Vapor
0.0	1.013E+03	299.70	26.55	2.448E+25	6.357E+23
1.0	9.040E+02	293.70	20.55	2.229E+25	4.349E+23
2.0	8.050E+02	287.70	14.55	2.027E+25	3.111E+23
3.0	7.150E+02	283.70	10.55	1.825E+25	1.572E+23
4.0	6.330E+02	277.00	3.85	1.655E+25	7.360E+22
5.0	5.590E+02	270.30	-2.85	1.498E+25	5.018E+22
6.0	4.920E+02	263.60	-9.55	1.352E+25	2.844E+22
7.0	4.320E+02	257.00	-16.15	1.218E+25	1.572E+22
8.0	3.780E+02	250.30	-22.85	1.094E+25	8.364E+21
9.0	3.290E+02	243.60	-29.55	9.782E+24	4.015E+21
10.0	2.860E+02	237.00	-36.15	8.741E+24	1.673E+21
11.0	2.470E+02	230.10	-43.05	7.775E+24	5.688E+20
12.0	2.130E+02	223.60	-49.55	6.900E+24	2.007E+20
13.0	1.820E+02	217.00	-56.15	6.075E+24	6.022E+19
14.0	1.560E+02	210.30	-62.85	5.373E+24	3.346E+19
15.0	1.320E+02	203.70	-69.45	4.694E+24	2.543E+19
16.0	1.100E+02	197.00	-76.15	4.044E+24	2.141E+19
17.0	9.370E+01	194.80	-78.35	3.484E+24	1.874E+19
18.0	7.890E+01	198.80	-74.35	2.875E+24	1.673E+19
19.0	6.660E+01	202.70	-70.45	2.380E+24	1.639E+19
20.0	5.650E+01	206.70	-66.45	1.980E+24	1.506E+19
21.0	4.800E+01	210.70	-62.45	1.650E+24	1.706E+19
22.0	4.090E+01	214.60	-58.55	1.380E+24	1.706E+19
23.0	3.500E+01	217.00	-56.15	1.168E+24	1.807E+19
24.0	3.000E+01	219.20	-53.95	9.913E+23	2.007E+19
25.0	2.570E+01	221.40	-51.75	8.408E+23	2.242E+19
30.0	1.220E+01	232.30	-40.85	3.804E+23	1.204E+19
35.0	6.000E+00	243.10	-30.05	1.788E+23	3.680E+18
40.0	3.000E+00	254.00	-19.15	8.555E+22	1.439E+18
45.0	1.600E+00	264.80	-8.35	4.377E+22	6.357E+17
50.0	9.000E-01	270.20	-2.95	2.413E+22	2.108E+17
70.0	5.200E-02	218.90	-54.25	1.721E+21	4.684E+15
100.0	3.200E-04	210.00	-63.15	1.104E+19	3.346E+13

Table 7. Moist Tropical Atmospheric Model

Altitude (km)	Pressure (Mb)	T (deg K)	T (deg C)	Number Density (m^{-3})	
				Total	Water Vapor
0.0	1.013E+03	296.20	23.05	2.477E+25	6.089E+23
1.0	9.031E+02	293.70	20.55	2.227E+25	4.781E+23
2.0	8.037E+02	287.70	14.55	2.023E+25	3.208E+23
3.0	7.136E+02	283.70	10.55	1.822E+25	2.332E+23
4.0	6.320E+02	277.00	3.85	1.653E+25	1.469E+23
5.0	5.580E+02	270.30	-2.85	1.495E+25	8.966E+22
6.0	4.911E+02	263.60	-9.55	1.349E+25	5.152E+22
7.0	4.308E+02	257.00	-16.15	1.214E+25	2.677E+22
8.0	3.765E+02	250.30	-22.85	1.090E+25	1.405E+22
9.0	3.279E+02	243.60	-29.55	9.750E+24	4.015E+21
10.0	2.844E+02	237.00	-36.15	8.692E+24	1.673E+21
11.0	2.457E+02	230.00	-43.15	7.738E+24	5.688E+20
12.0	2.130E+02	223.60	-49.55	6.900E+24	2.007E+20
13.0	1.820E+02	217.00	-56.15	6.075E+24	6.022E+19
14.0	1.560E+02	210.30	-62.85	5.373E+24	3.346E+19
15.0	1.335E+02	203.65	-69.50	4.748E+24	2.743E+19
16.0	1.110E+02	197.00	-76.15	4.081E+24	2.141E+19
17.0	9.495E+01	197.90	-75.25	3.475E+24	1.907E+19
18.0	7.890E+01	198.80	-74.35	2.875E+24	1.673E+19
19.0	6.770E+01	202.75	-70.40	2.419E+24	1.589E+19
20.0	5.650E+01	206.70	-66.45	1.980E+24	1.506E+19
21.0	4.800E+01	210.70	-62.45	1.650E+24	1.706E+19
22.0	4.090E+01	214.60	-58.55	1.380E+24	1.706E+19
23.0	3.500E+01	217.00	-56.15	1.168E+24	1.807E+19
24.0	3.000E+01	219.20	-53.95	9.913E+23	2.007E+19
25.0	2.570E+01	221.40	-51.75	8.408E+23	2.242E+19
30.0	1.220E+01	232.30	-40.85	3.804E+23	1.204E+19
35.0	6.000E+00	243.10	-30.05	1.788E+23	3.680E+18
40.0	3.050E+00	254.00	-19.15	8.697E+22	1.439E+18
45.0	1.590E+00	264.80	-8.35	4.349E+22	6.357E+17
50.0	8.540E-01	270.20	-2.95	2.289E+22	2.108E+17
70.0	5.200E-02	218.90	-54.25	1.721E+21	4.684E+15
100.0	3.200E-04	210.00	-63.15	1.104E+19	3.346E+13

Table 8. Desert Atmospheric Model

Altitude (km)	Pressure (Mb)	T (deg K)	T (deg C)	Number Density (m^{-3})	
				Total	Water Vapor
0.0	1.009E+03	304.05	30.90	2.404E+25	1.974E+23
1.0	9.013E+02	297.95	24.80	2.191E+25	1.572E+23
2.0	8.029E+02	291.75	18.60	1.993E+25	1.171E+23
3.0	7.134E+02	285.55	12.40	1.810E+25	7.695E+22
4.0	6.323E+02	279.45	6.30	1.639E+25	5.353E+22
5.0	5.588E+02	273.45	0.30	1.480E+25	3.346E+22
6.0	4.926E+02	267.45	-5.70	1.334E+25	1.539E+22
7.0	4.329E+02	261.55	-11.60	1.199E+25	1.104E+22
8.0	3.793E+02	255.25	-17.90	1.076E+25	7.360E+21
9.0	3.312E+02	248.55	-24.60	9.652E+24	5.018E+21
10.0	2.882E+02	241.65	-31.50	8.638E+24	2.543E+21
11.0	2.497E+02	234.45	-38.70	7.714E+24	5.688E+20
12.0	2.153E+02	226.55	-46.60	6.883E+24	3.212E+20
13.0	1.846E+02	218.75	-54.40	6.112E+24	1.539E+20
14.0	1.575E+02	211.25	-61.90	5.400E+24	6.022E+19
15.0	1.353E+02	206.75	-66.40	4.740E+24	4.282E+19
16.0	1.131E+02	202.25	-70.90	4.050E+24	2.509E+19
17.0	9.670E+01	200.50	-72.65	3.493E+24	2.108E+19
18.0	8.030E+01	198.75	-74.40	2.926E+24	1.706E+19
19.0	6.880E+01	202.60	-70.55	2.460E+24	1.606E+19
20.0	5.730E+01	206.45	-66.70	2.010E+24	1.506E+19
21.0	4.860E+01	210.45	-62.70	1.673E+24	1.706E+19
22.0	4.140E+01	214.25	-58.90	1.400E+24	1.706E+19
23.0	3.530E+01	216.85	-56.30	1.179E+24	1.807E+19
24.0	3.020E+01	219.05	-54.10	9.986E+23	2.007E+19
25.0	2.590E+01	221.25	-51.90	8.479E+23	2.242E+19
30.0	1.220E+01	232.35	-40.80	3.803E+23	1.204E+19
35.0	5.900E+00	243.35	-29.80	1.756E+23	3.680E+18
40.0	3.000E+00	254.05	-19.10	8.553E+22	1.439E+18
45.0	1.500E+00	265.05	-8.10	4.099E+22	6.022E+17
50.0	8.000E-01	269.95	-3.20	2.147E+22	2.242E+17
70.0	5.200E-02	217.80	-55.35	1.729E+21	4.015E+15
100.0	3.200E-04	210.40	-62.75	1.102E+19	2.275E+14

Table 9. 1976 U.S. Standard Atmospheric Model

Altitude (km)	Pressure (Mb)	T (deg K)	T (deg C)	Number Density (m^{-3})	
				Total	Water Vapor
0.0	1.013E+03	288.20	15.05	2.546E+25	1.937E+23
1.0	8.988E+02	281.70	8.55	2.311E+25	1.235E+23
2.0	7.950E+02	275.20	2.05	2.092E+25	7.628E+22
3.0	7.012E+02	268.70	-4.45	1.890E+25	4.216E+22
4.0	6.166E+02	262.20	-10.95	1.703E+25	2.288E+22
5.0	5.405E+02	255.70	-17.45	1.531E+25	1.181E+22
6.0	4.722E+02	249.20	-23.95	1.372E+25	6.189E+21
7.0	4.111E+02	242.70	-30.45	1.227E+25	3.011E+21
8.0	3.565E+02	236.20	-36.95	1.093E+25	1.509E+21
9.0	3.080E+02	229.70	-43.45	9.712E+24	5.052E+20
10.0	2.650E+02	223.30	-49.85	8.596E+24	1.726E+20
11.0	2.270E+02	216.80	-56.35	7.584E+24	6.825E+19
12.0	1.940E+02	216.70	-56.45	6.484E+24	2.636E+19
13.0	1.658E+02	216.70	-56.45	5.542E+24	1.101E+19
14.0	1.417E+02	216.70	-56.45	4.736E+24	4.416E+18
15.0	1.211E+02	216.70	-56.45	4.048E+24	2.720E+18
16.0	1.035E+02	216.70	-56.45	3.459E+24	1.576E+18
17.0	8.850E+01	216.70	-56.45	2.958E+24	1.124E+18
18.0	7.565E+01	216.70	-56.45	2.529E+24	8.197E+17
19.0	6.467E+01	216.70	-56.45	2.162E+24	6.056E+17
20.0	5.529E+01	216.70	-56.45	1.848E+24	4.483E+17
21.0	4.729E+01	217.60	-55.55	1.574E+24	3.339E+17
22.0	4.047E+01	218.60	-54.55	1.341E+24	2.493E+17
23.0	3.467E+01	219.60	-53.55	1.144E+24	1.884E+17
24.0	2.972E+01	220.60	-52.55	9.758E+23	1.412E+17
25.0	2.549E+01	221.60	-51.55	8.332E+23	1.067E+17
30.0	1.197E+01	226.50	-46.65	3.828E+23	2.472E+16
35.0	5.746E+00	236.50	-36.65	1.760E+23	5.654E+15
40.0	2.871E+00	250.40	-22.75	8.305E+22	1.362E+15
45.0	1.491E+00	264.20	-8.95	4.088E+22	3.613E+14
50.0	7.980E-01	270.70	-2.45	2.135E+22	1.010E+14
70.0	5.200E-02	219.70	-53.45	1.714E+21	4.015E+11
100.0	3.200E-04	210.00	-63.15	1.104E+19	2.232E+06